The residual-based variational multiscale formulation for the large eddy simulation of compressible flows

J. Liu and A. A. Oberai

Department of Mechanical, Aerospace and Nuclear Engineering,

Rensselaer Polytechnic Institute,

Troy, NY 12180, U.S.A.

Phone: 518 276 3386, Fax: 518 276 3055, Email: oberaa@rpi.edu

Abstract

The residual-based variational multiscale formulation is applied to develop a large eddy simulation (LES) model for compressible flows. In addition, a mixed model, in which a deviatoric Smagorinsky subgrid stress term is added to the RBVM terms to better model the Reynolds stresses is proposed. These models, along with the dynamic Smagorinsky-Yoshizawa-eddy diffusivity model are tested in predicting the decay of homogenous turbulence. For most relevant measures, it is observed that the RBVM models are more accurate than the dynamic Smagorinsky-type model.

Keywords: Residual-based variational multiscale formulation, Large eddy simulation, Compressible flows

1 Introduction

In large eddy simulation (LES) the large scales of fluid motion are explicitly resolved while the effect of the fine scales on the large scales is modeled using terms that depend solely on the large scale variables. In filter-based LES this scale separation is achieved through the application of spatial filters that tend to smooth a given field variable. In contrast to this in the variational multiscale (VMS) formulation the scale separation is achieved through projection operators [1]. In addition in the VMS formulation the starting point for deriving LES models is the weak or the variational statement of conservation laws, whereas in the filter-based LES formulation it is the strong form of these equations.

In the residual-based variational multiscale (RBVM) formulation [2, 3] the basic idea is to split the solution and weighting function spaces into coarse and fine scale partitions. Splitting the weighting functions in this way yields two sets of coupled equations: one for the coarse scales and another for the fine, or the unresolved, scales. The equations for the fine scales are observed to be driven by the residual of the coarse scale solution projected onto the fine scale space. Hence the name the "residual-based" VMS formulation. These equations for the unresolved scales are solved approximately and the solution is substituted in the equations for the coarse scales. In this way the effect of the fine or the unresolved scales on the coarse scales is modeled.

Thus far the RBVM formulation has been applied to incompressible turbulent flows [2, 4, 5, 6] and variable density turbulent flows [7]. In this context in [8, 9] it was

observed that while the RBVM formulation accurately modeled the cross-stress terms ($\bar{u}u'$ terms) it did not at all model the Reynolds stress terms ($u'u'$). To remedy this a mixed model was proposed that appended to the RBVM terms a Smagorinsky eddy viscosity model [10] in order to capture the effect of the Reynolds stresses. The value of the Smagorinsky parameter in this model was determined dynamically, while accounting for the dissipation induced by the RBVM terms. In tests of the decay of incompressible homogeneous turbulence it was observed that the mixed model was more accurate than the RBVM and the dynamic Smagorinsky models.

In this paper we aim to extend these ideas to compressible turbulent flows. First, we consider the extension of the RBVM formulation to compressible flows. Thereafter motivated by the shortcomings of this model in the incompressible case we consider a mixed version of this model where we add the Smagorinsky, Yoshizawa [11], and eddy diffusivity terms to model the Reynolds components of the deviatoric subgrid stresses, the dilatational subgrid stresses and the subgrid heat flux vector, respectively [12]. Through a simple analysis of the subgrid mechanical energy and through the dynamic approach we conclude that out of these the RBVM formulation requires a model only for the deviatoric component of the Reynolds stresses. The other significant subgrid quantities are adequately represented within the RBVM formulation. Thus the mixed RBVM formulation for compressible flows contains only one additional term when compared with the RBVM formulation, which is the deviatoric Smagorinsky model.

We test the performance of all LES models (RBVM, mixed and dynamic Smagorinsky-

Yoshizawa-eddy diffusivity model) in predicting the decay of compressible homogeneous turbulence. In order to ensure that the compressible effects are significant, and at the same time the flow is not overwhelmed by strong shocks we select flow parameters such that weak, local shocks, called shocklets are observed [13, 14, 15]. We compare all models against fully resolved direct numerical simulations (DNS) and conclude that the RBVM and the mixed model are more accurate than the dynamic Smagorinsky-type model.

The RBVM models appear to be endowed with a built-in "dynamic" feature. In particular, in regions of the flow where the solution is smooth and is accurately represented by the coarse scales, the residual of the coarse scale tends to be small. As a result the fine scales, which are driven by the coarse-scale residual, are weak and all the model terms tend to vanish. This has allowed practitioners to implement these models with no dynamic procedures which are necessary for other Smagorinsky-type models. We note that there is another version of the VMS formulation where the resolved scales are further split into coarse and fine scales and eddy viscosity-type models are used to model the effect of the unresolved scales only in the equations for the fine scales [16, 17]. No models are introduced in the equations for the coarse resolved scales.

In addition to the VMS approach, there are several other LES methods that are based on utilizing multiscale ideas. These include scale similarity model, where the subgrid stress at the grid level is assumed to be proportional to the subgrid stress evaluated at a coarser level (which is calculable) [18]. This yields an explicit expression for the subgrid stress which is, however, unstable on its own and is often appended with

a Smagorinsky-type term to yield a stable model [19, 20, 21, 22]. In the approximate deconvolution model (ADM), an approximation for the unfiltered velocity is constructed using the filtered velocity field and is used to reconstruct the subgrid tensor [23, 24]. In this case also, a purely dissipative relaxation term is added in order to complete the model. Similar ideas for reconstructing the fine scale velocity field are also employed in the subgrid scale estimation model within the context of the truncated Navier-Stokes equations [25]. The RBVM approach is related to these models in that it relies on reconstructing the entire velocity field (fine and coarse scale components) and using it to model the subgrid stresses. There are however significant differences that are derived from the fact that the RBVM approach relies on using projections and not filters, and as a result the fine scale velocity is proportional to the residual of the coarse scale solution.

The layout of the reminder of this paper is as follows. In the following section, the RBVM formulation for compressible flows is derived. In Section 3, the mixed model based on the RBVM formulation is presented and analyzed. In Section 4 these models are specialized to the case of Fourier-spectral discretization and in Section 5 they are tested in predicting the decay of homogeneous turbulence of compressible fluids. Conclusions are drawn in Section 6.

2 Residual-based variational multiscale formulation

In this section, the RBVM formulation of LES for the compressible Navier-Stokes equations is developed. For a detailed derivation of the RBVM approach for the incompressible Navier-Stokes equations the reader is referred to [2].

The strong form of the compressible Navier–Stokes equations in dimensionless variables is given by

$$\frac{\partial \rho}{\partial t} + \nabla \cdot \boldsymbol{m} = 0 \tag{1}$$

$$\frac{\partial \boldsymbol{m}}{\partial t} + \nabla \cdot (\frac{\boldsymbol{m} \otimes \boldsymbol{m}}{\rho}) = -\nabla p + \frac{1}{Re} \nabla \cdot \boldsymbol{\sigma} + \boldsymbol{f} \tag{2}$$

$$\frac{\partial p}{\partial t} + \nabla \cdot (\boldsymbol{u} p) + (\gamma - 1) p \nabla \cdot \boldsymbol{u} = \frac{(\gamma - 1)}{Re} \Phi + \frac{1}{M_\infty^2 Pr Re} \nabla \cdot (\mu \nabla T) \tag{3}$$

where the viscous stress tensor $\boldsymbol{\sigma}$ is given in terms of the rate of strain $\boldsymbol{S}$ by

$$\boldsymbol{\sigma} = 2\mu (\boldsymbol{S} - \frac{1}{3} tr(\boldsymbol{S}) \boldsymbol{I}) \tag{4}$$

and the viscous dissipation Φ is given by

$$\Phi = \boldsymbol{\sigma} : \boldsymbol{S} \ . \tag{5}$$

The system is closed with an equation of state

$$\gamma M_\infty^2 p = \rho T \ . \tag{6}$$

Further, the dynamic viscosity is expressed in terms of the local temperature using,

$$\mu = T^{0.76}. \tag{7}$$

This problem is posed on a spatial domain Ω and in the time interval $]0, T[$ with given initial condition data and boundary conditions. In the above equations, ρ is the

density, $\boldsymbol{u}$ is the velocity, $\boldsymbol{m} = \rho\boldsymbol{u}$ is the momentum, p is the thermal pressure, T is temperature, M_∞ is the free-stream Mach number, γ is the adiabatic index, Pr is the Prandtl number, Re is the Reynolds number and $\boldsymbol{f}$ is a forcing function. The density, velocity, temperature and viscosity are scaled by their reference values while the pressure is scaled by the product of the reference density and the square of the reference velocity. The Reynolds number is based on the reference values of the velocity, length, viscosity and density. For the homogeneous turbulence problem considered in this paper, the flow is assumed to be periodic with a period 2π in each coordinate direction. The values of the physical parameters are provided in Section 4.

Note that one can write (1),(2) and (3) concisely as

$$\mathcal{L}\boldsymbol{U} = \boldsymbol{F}, \tag{8}$$

where $\boldsymbol{U} = [\rho,\ \boldsymbol{m},\ p]^T$ are the unknowns, $\boldsymbol{F} = [0,\ \boldsymbol{f},\ 0]^T$ and $\mathcal{L}$ represents the differential operator associated with the Navier–Stokes equations.

The weak form of $(1) - (3)$ is given by: Find $\boldsymbol{U} \in \mathcal{V}$ such that

$$A(\boldsymbol{W}, \boldsymbol{U}) = (\boldsymbol{W}, \boldsymbol{F}) \qquad \forall \boldsymbol{W} \in \mathcal{V}. \tag{9}$$

Here $A(\cdot, \cdot)$ is a semi-linear form that is linear in its first slot, $(\cdot, \cdot)$ denotes the L_2 inner product, $\boldsymbol{W} = [r, \boldsymbol{w}, q]^T$ is the weighting function, $\mathcal{V}$ is the space of trial solutions and

weighting functions. The semi-linear form is given by

$$\begin{aligned} A(\boldsymbol{W},\boldsymbol{U}) \quad \equiv \quad & (r,\rho_{,t}) - (\nabla r,\boldsymbol{m}) \\ & + (\boldsymbol{w},\boldsymbol{m}_{,t}) - (\nabla \boldsymbol{w},\frac{\boldsymbol{m}\otimes\boldsymbol{m}}{\rho}) \\ & - (\nabla\cdot\boldsymbol{w},p) + \frac{1}{Re}(\nabla\boldsymbol{w},\boldsymbol{\sigma}) \\ & + (q,p_{,t}) - (\nabla q,\boldsymbol{u}p) - (1-\gamma)(q,p\nabla\cdot\boldsymbol{u}) \\ & - \frac{(\gamma-1)}{Re}(q,\Phi) + \frac{1}{M_\infty^2 PrRe}(\nabla q,\mu\nabla T)\ . \end{aligned} \tag{10}$$

The weak form is posed using the infinite dimensional function space $\mathcal{V}$. In practice this space is approximated by its finite-dimensional counterpart $\mathcal{V}^h \subset \mathcal{V}$. In the residual-based variational multiscale formulation the goal is to construct a finite dimensional problem whose solution is equal to $\mathbb{P}^h\boldsymbol{U}$, where $\mathbb{P}^h : \mathcal{V} \to \mathcal{V}^h$ is a projection operator that defines the desired or optimal solution. If the range of $\mathbb{P}^h$ is all of $\mathcal{V}^h$ then it is possible to split $\mathcal{V} = \mathcal{V}^h \oplus \mathcal{V}'$ which implies that for every $\boldsymbol{V} \in \mathcal{V}$ there is a unique decomposition $\boldsymbol{V} = \boldsymbol{V}^h + \boldsymbol{V}'$, where $\boldsymbol{V}^h = \mathbb{P}^h\boldsymbol{V} \in \mathcal{V}^h$ and $\boldsymbol{V}' = \mathbb{P}'\boldsymbol{V} \in \mathcal{V}'$. The space $\mathcal{V}' \equiv \{\boldsymbol{V} \in \mathcal{V} | \mathbb{P}^h\boldsymbol{V} = \boldsymbol{0}\}$, and $\mathbb{P}' = \mathbb{I} - \mathbb{P}^h$ where $\mathbb{I}$ is the identity operator. Using this decomposition in (9) for both the weighting functions and the trial solutions we arrive at a set of coupled equations. Find $\boldsymbol{U}^h \in \mathcal{V}^h$ and $\boldsymbol{U}' \in \mathcal{V}'$, such that

$$A(\boldsymbol{W}^h,\boldsymbol{U}^h+\boldsymbol{U}') = (\boldsymbol{W}^h,\boldsymbol{F}) \qquad \forall \boldsymbol{W}^h \in \mathcal{V}^h, \tag{11}$$

$$A(\boldsymbol{W}',\boldsymbol{U}^h+\boldsymbol{U}') = (\boldsymbol{W}',\boldsymbol{F}) \qquad \forall \boldsymbol{W}' \in \mathcal{V}'. \tag{12}$$

The idea is to solve for $\boldsymbol{U}'$ in terms of $\boldsymbol{U}^h$ and $\boldsymbol{F}$ analytically using the fine scale equation (12), and substitute the expression for $\boldsymbol{U}'$ into the coarse-scale equation (11),

which is to be solved numerically. By doing this one would have introduced in the coarse scale equation the effect of the fine or subgrid scales.

To derive an expression for $\boldsymbol{U}'$ we subtract $A(\boldsymbol{W}', \boldsymbol{U}^h)$ from both sides of (12),

$$\begin{aligned} A(\boldsymbol{W}', \boldsymbol{U}^h + \boldsymbol{U}') - A(\boldsymbol{W}', \boldsymbol{U}^h) &= -A(\boldsymbol{W}', \boldsymbol{U}^h) + (\boldsymbol{W}', \boldsymbol{F}) \\ &= -(\boldsymbol{W}', \mathcal{L}\boldsymbol{U}^h - \boldsymbol{F}), \end{aligned} \tag{13}$$

where we have performed integration by parts on the first term on the right hand side of the first line of (13). For general functions in $H^1(\Omega)$ the quantity $\mathcal{L}\boldsymbol{U}^h$ must be interpreted in the sense of distributions. Note that this equation for $\boldsymbol{U}'$ is driven by the coarse-scale residual $\mathcal{R}(\boldsymbol{U}^h) \equiv \mathcal{L}\boldsymbol{U}^h - \boldsymbol{F}$. Further, when the coarse-scale residual is zero its solution is given by $\boldsymbol{U}' = \boldsymbol{0}$. The formal solution of (13) may be written as

$$\boldsymbol{U}' = \mathcal{F}'(\mathcal{R}(\boldsymbol{U}^h); \boldsymbol{U}^h). \tag{14}$$

This implies that the fine scales are a functional of the residual of the coarse scales and are parameterized by the coarse scales. Thus they depend on the entire history of the coarse scales and their residual. A short-time approximation that does away with all the history effects and replaces the differential operator in (13) by an algebraic operator is given by

$$\boldsymbol{U}' \approx -\mathbb{P}'\boldsymbol{\tau}(\boldsymbol{U}^h)\, \mathbb{P}'^T \mathcal{R}(\boldsymbol{U}^h). \tag{15}$$

Here $\mathbb{P}'^T : \mathcal{V}^{h*} \to \mathcal{V}^*$ is the transpose of $\mathbb{P}'$, where the spaces $\mathcal{V}^{h*}$ and $\mathcal{V}^*$ are dual of $\mathcal{V}^h$ and $\mathcal{V}$, respectively, with respect to the L_2 duality pairing [26]. Further, $\boldsymbol{\tau}$ is a matrix that depends on $\boldsymbol{U}^h$. The operator $\boldsymbol{\tau}$ is selected to approximate the Green's operator

for the fine-scale problem, and can be thought of as a double integral of the Green's operator. In moving from (14) to (15) instead of solving a very complicated equation for the fine scales, a gross approximation is made. In particular it is assumed that the fine scales are equal to the residual of the coarse scales, which represent the rate of unbalance for the coarse scale representation of a given conservation variable, times the characteristic time scale. In the advective limit this time scale is the time it takes to advect the fine scale scales across a typical grid size, and in the diffusive limit it is the time it takes for them to diffuse. The precise definition of $\boldsymbol{\tau}$ is presented in Section 4. For a discussion on this the reader is referred to [1, 2]. The approximation for $\boldsymbol{U}'$ above differs from that in [2] in the inclusion of the projectors $\mathbb{P}'$ and $\mathbb{P}'^T$. We believe that these projectors are necessary in order to maintain a formal consistency between the exaction equation for the fine scales (13) and its approximation (15). In particular the operator $\mathbb{P}'^T$ ensures that any component of the residual that is not "sensed" by a function in $\mathcal{V}'$ does not contribute to the fine scales, and the operator $\mathbb{P}'$ ensures that the approximation for the fine scales belongs to $\mathcal{V}'$. In this regard the approximation above is closer to the orthogonal sub-scales method of Codina [3].

Using this expression in (11) we arrive at the equation for the residual-based variational multiscale (RBVM) formulation: Find $\boldsymbol{U}^h \in \mathcal{V}^h$, such that

$$A(\boldsymbol{W}^h, \boldsymbol{U}^h - \mathbb{P}'\boldsymbol{\tau}\,\mathbb{P}'^T\mathcal{R}(\boldsymbol{U}^h)) = (\boldsymbol{W}^h, \boldsymbol{F}) \qquad \forall \boldsymbol{W}^h \in \mathcal{V}^h. \tag{16}$$

Remark: The space for $\boldsymbol{U}'$, that is $\mathcal{V}'$, is infinite dimensional. However, in practice this space must also be approximated with a finite dimensional space. Furthermore it

must be selected such that the cost of computing $\boldsymbol{U}'$ in this space does not overwhelm the total computational costs. In our application, where we have used Fourier modes, the coarse scale space is comprised of all modes with wavenumber less than or equal to the cutoff wavenumber k^h, and *the fine scale space is comprised of all modes with wavenumber greater than* k^h *but less than or equal to* $\frac{3k^h}{2}$. This choice is motivated by tests (not shown here) that have shown that using a fine scale space that is larger than this does not significantly alter the results. Thus in order to minimize the computational effort we select the smallest possible space for $\boldsymbol{U}'$. We note that the ratio of memory costs for the RBVM model to the no-model case scales as α^3, where $\alpha > 1$ is the ratio of the cutoff wavenumber for the fine scales to the coarse scales. The ratio of flops per time-step also scales with the same power of α. Therefore it is imperative that α be kept small in order for the RBVM formulation to be competitive.

3 A mixed model

3.1 A mixed model based on RBVM formulation

In [9], for incompressible flows the authors demonstrated that while the RBVM model works well for the cross-stress term it does not introduce an adequate model for the Reynolds stress term. Subsequent analysis has revealed that the RBVM approximation for the fine scales produces a reasonable estimate for their magnitude [27, 28]. Thus the reason why the Reynolds stresses are not accurately represented is not because their magnitude is underestimated, rather it is that they are uncorrelated with the large-scale

rate of strain tensor. A likely explanation for this is the exclusion of the history effects in the approximation for the fine scales which prevents these correlations from evolving. With this in mind they appended to the RBVM model the dynamic Smagorinsky model in order to model the Reynolds stress. We follow the same approach and propose the following mixed model for compressible flows: Find $\boldsymbol{U}^h \in \mathcal{V}^h$, such that

$$
\begin{aligned}
& A\big(\boldsymbol{W}^h, \boldsymbol{U}^h + \boldsymbol{U}'\big) \\
& + \big(\nabla \boldsymbol{w}^h, \quad 2C_0 h^2 \rho^h |\boldsymbol{S}^h| \boldsymbol{S}^h_{dev} - \frac{2}{3} C_1 h^2 \rho^h |\boldsymbol{S}^h|^2 \boldsymbol{I}\big) \\
& + \big(\nabla q^h, \quad \frac{C_0}{Pr_t \gamma M_\infty^2} h^2 \rho^h |\boldsymbol{S}^h| \nabla T^h\big) \\
& \qquad\qquad = (\boldsymbol{W}^h, \boldsymbol{F}) \quad \forall \boldsymbol{W}^h \in \mathcal{V}^h \ ,
\end{aligned}
\tag{17}
$$

where $A(\cdot,\cdot)$ is defined in (10), $\boldsymbol{S}^h$ is the rate of strain computed the velocity field $\boldsymbol{u}^h \equiv \frac{\boldsymbol{m}^h}{\rho^h}$, the subscript dev denotes its deviatoric component and $T^h \equiv \frac{\gamma M_\infty^2 p^h}{\rho^h}$. From the definitions of $\boldsymbol{u}^h$ and T^h we note that these correspond to the so-called Favre-averaged variables in traditional LES nomenclature.

Comparing with (16), we note that two new terms have been added. The first term models the deviatoric and dilatational components of the subgrid scale stress tensor and the second term models the subgrid heat flux vector. For the deviatoric component of the subgrid stress we have utilized the Smagorinsky eddy viscosity model [10], for the dilatational component we have utilized Yoshizawa's model [11], and for the subgrid heat flux vector we have utilized an eddy diffusivity type model. In a typical LES the first term is employed to represent both the cross and Reynolds stress components of

the subgrid stress, whereas in our mixed model it is added to represent the missing Reynolds stress. In the following section we demonstrate that the RBVM model by itself introduces a reasonable expression for the dilatational Reynolds stress component. Based on this analysis we do not include an eddy viscosity model for the dilatational component of subgrid stress (that is $C_1 = 0$). Further in Section 4 we note that the dynamic procedure yields a negative value for Pr_t^{-1} which is clipped to zero. Thus in effect in the mixed model $C_1 = Pr_t^{-1} = 0$ and the only non-zero term corresponds to C_0, that is a model for the deviatoric subgrid stresses.

3.2 Analysis of mechanical energy for the RBVM formulation

In this section we derive a mechanical energy identity for the RBVM formulation. We split the total rate transfer of mechanical energy due to the subgrid scales into a dilatational and deviatoric component. For the deviatoric component, in earlier studies of incompressible flows it has been shown that the RBVM model is unable to model the Reynolds stress term, and for this purpose a mixed model is necessary. For the dilatational component, we demonstrate that the RBVM model introduces a cross and a Reynolds-stress term, where the latter is similar to the Yoshizawa model. As a result no additional model is required for the dilatational component of the stress tensor.

We begin by noting that (17) contains all the models considered in the manuscript. In particular when $\boldsymbol{U}' = \mathbf{0}$ and $C_1 = C_0 = 0$, it represents the Galerkin method, or the DNS case; when only $\boldsymbol{U}' = \mathbf{0}$ it reduces to the Smagorinsky-Yoshizawa model; when $C_1 = C_0 = 0$, it reduces to the RBVM model; when all terms are active it represents

the mixed model.

Setting $\boldsymbol{W}^h = [0, \boldsymbol{u}^h, 0]^T$ in this equation for the Galerkin method we arrive at mechanical energy identity:

$$\frac{d}{dt}\Big(\frac{1}{2}\int_\Omega \rho^h |\boldsymbol{u}^h|^2 dx\Big) = \overbrace{-\int_\Omega \frac{|\boldsymbol{u}^h|^2}{2}\big(\rho^h_{,t} + \nabla\cdot(\rho^h\boldsymbol{u}^h)\big)dx - \int_\Omega \boldsymbol{S}^h : \boldsymbol{\sigma}^h_t dx}^{\equiv \epsilon^h_{Gal}}, \tag{18}$$

where $\boldsymbol{\sigma}^h_t = -p^h\mathbf{1} + \frac{1}{Re}\boldsymbol{\sigma}^h$ is the total Cauchy stress tensor. This equation states that the rate of change of kinetic energy is determined by the dissipation induced by the molecular stresses and a term that depends on the residual of the continuity equation. We combine these two contributions into a term denoted by ϵ^h_{Gal}.

Next we consider (17) written for the Smagorinsky-Yoshizawa model and set $\boldsymbol{W}^h = [0, \boldsymbol{u}^h, 0]^T$ to arrive at the mechanical energy identity for this model:

$$\frac{d}{dt}\Big(\frac{1}{2}\int_\Omega \rho^h |\boldsymbol{u}^h|^2 dx\Big) = \epsilon^h_{Gal} - 2C_0h^2\int_\Omega \rho^h |\boldsymbol{S}^h||\boldsymbol{S}^h_{dev}|^2 dx + \frac{2}{3}C_1h^2\int_\Omega \rho^h |\boldsymbol{S}^h|^2(\nabla\cdot\boldsymbol{u}^h)dx, \tag{19}$$

where $\boldsymbol{S}^h_{dev}$ denotes the deviatoric part of $\boldsymbol{S}^h$. From this equation we conclude that the deviatoric contribution to the rate of change of kinetic energy is negative and thus this term always dissipates resolved kinetic energy. On the other hand, the dilatational contribution can either add or remove kinetic energy. When $\nabla\cdot\boldsymbol{u}^h < 0$, that is we have a flow where resolved scales are undergoing a compression, this term is negative and as a result the resolved scales loose kinetic energy. The situation is reversed in the case of an expansion.

Finally we consider (17) written for the RBVM model and set $\boldsymbol{W}^h = [0, \boldsymbol{u}^h, 0]^T$ to

arrive at the mechanical energy identity:

$$\begin{aligned}\frac{d}{dt}\Big(\frac{1}{2}\int_\Omega \rho^h|\boldsymbol{u}^h|^2dx\Big) \;\approx\; & \epsilon^h_{Gal} \\ & -\int_\Omega \rho^h \boldsymbol{S}^h_{dev} : (\boldsymbol{u}^h\otimes\boldsymbol{u}' + \boldsymbol{u}'\otimes\boldsymbol{u}^h + \boldsymbol{u}'\otimes\boldsymbol{u}')_{dev}dx \\ & +\frac{1}{3}\int_\Omega \rho^h(\nabla\cdot\boldsymbol{u}^h)(2\boldsymbol{u}^h\cdot\boldsymbol{u}' + |\boldsymbol{u}'|^2)dx \end{aligned} \tag{20}$$

We have used the $\approx$ symbol above to indicate that we are only considering the dominant RBVM model terms in this equation. The second line of (20) contains the RBVM contributions to the deviatoric portion of the subgrid stress, while the third line contains the contributions to the dilatational portion. Further, in both these lines the last term is the Reynolds stress term. We note that there is a significant difference in the structure of the Reynolds stress terms. In the deviatoric case this term is such that it must rely on correlations between $\boldsymbol{u}'$ and $\boldsymbol{u}^h$ to ensure that $\boldsymbol{S}^h_{dev} : (\boldsymbol{u}'\otimes\boldsymbol{u}')_{dev} > 0$ at most spatial locations so that the integral will be dissipative overall. As mentioned in Section 3 the approximation for $\boldsymbol{u}'$ calculated using the RBVM approximation does not achieve this. On the other hand, in the dilatational case, *regardless of the correlations between* $\boldsymbol{u}'$ *and* $\boldsymbol{u}^h$ *the Reynolds stress term is such that it always extracts energy from the the coarse scales when they are undergoing a compression, and adds energy when they expand.* In this regard it is exactly like the Smagorinsky-Yoshizawa model. This implies that the RBVM model for the dilatational component of the Reynolds stress will be effective as along as the magnitude of $\boldsymbol{u}'$ is evaluated accurately. Thus it would appear that in the mixed model it is not necessary to add the Smagorinsky component to the dilatational portion of subgrid stresses. So in our mixed model $C_1 = 0$, while C_0 and Pr_t are

determined dynamically.

Summary All models described in this paper and tested in the following section are contained in (17) (see also Table 1). For a direct numerical simulation there are no model terms, so in this equation $\boldsymbol{\tau} = \mathbf{0}$ and $C_0 = C_1 = 0$. For the dynamic Smagorinsky-Yoshizawa-eddy diffusivity model (DSYE) the fine scale solution is zero, so $\boldsymbol{\tau} = \mathbf{0}$ and C_0, C_1 and Pr_t are determined dynamically using the variational counterpart of the Germano identity [29, 30] (see Appendix A). For the residual based variational multiscale model (RBVM) the fine scales are active, that is $\boldsymbol{\tau} \neq \mathbf{0}$ while $C_0 = C_1 = 0$. For the mixed model the fine scales are active $\boldsymbol{\tau} \neq \mathbf{0}$, $C_1 = 0$, while C_0 and Pr_t are determined dynamically (see Appendix A). In our simulation of the decay of compressible turbulence using the mixed model we have found that dynamic procedure almost always yields negative values for Pr_t, indicating that RBVM model alone introduces adequate dissipation in the energy equation. In order to avoid unstable solutions we set $Pr_t^{-1} = 0$ whenever this happens. The net result is that in the mixed model the only active term is Smagorinsky model for the deviatoric component of the subgrid stress.

Remark We note that our mixed model is similar to other mixed models, including the scale-similarity model [18, 31, 19, 21] and the tensor-diffusivity model [32, 33] in that it contains distinct models for the cross-stress term and the Reynolds stress term. However, the form of the model term for the cross stress in our model is distinct from other mixed models.

Table 1: A concise description of all models based on the terms appearing in (17).

Terms	No Model	Smagorinsky-Yoshizawa	RBVM	Mixed
$\boldsymbol{\tau}$	$\mathbf{0}$	$\mathbf{0}$	✓	✓
C_0	0	✓	0	✓
C_1	0	✓	0	0
Pr_t^{-1}	0	✓	0	0

4 Specialization to a Fourier spectral basis

We apply the formulation developed in the previous section in order to simulate the decay of homogeneous isotropic turbulence of compressible flows. We assume that $\Omega = \ ]0, 2\pi[^3$ and the density, velocity and pressure fields satisfy periodic boundary conditions. We propose to simulate this problem using the Fourier-spectral method. In this case the space of functions $\mathcal{V}^h$ are approximated by a Fourier-spectral basis. Fourier modes with $|\boldsymbol{k}| < k^h$ are used to define $\mathcal{V}^h$. We note that these basis functions have the special property that they are orthogonal to each other in all H^m inner-products. In addition, we define the projector $\mathbb{P}^h$ to be the H^1 projection and due to the orthogonality of the Fourier modes this is the low-pass sharp cut-off filter in wavenumber space. Then $\mathbb{P}'$ and $\mathbb{P}'^T$ are the high-pass, sharp cutoff filter in wavenumber space.

As a result of this, the equations for the LES model derived in the previous section

simplify to

$$\frac{\partial \widehat{\rho}^h}{\partial t} + i\boldsymbol{k}\cdot\widehat{\boldsymbol{m}}^h = 0 \tag{21}$$

$$\frac{\partial \widehat{\boldsymbol{m}}^h}{\partial t} + i\boldsymbol{k}\cdot\frac{\widehat{\boldsymbol{m}\otimes\boldsymbol{m}}}{\rho} + i\boldsymbol{k}\widehat{p}^h = \frac{1}{Re}i\boldsymbol{k}\cdot\widehat{\boldsymbol{\sigma}} + i\boldsymbol{k}\cdot 2C_0h^2\rho^h\widehat{|\boldsymbol{S}^h|\boldsymbol{S}^h_{dev}} - i\boldsymbol{k}\frac{2}{3}C_1h^2\widehat{\rho^h|\boldsymbol{S}^h|^2} \tag{22}$$

$$\frac{\partial \widehat{p}^h}{\partial t} + i\boldsymbol{k}\cdot\widehat{\boldsymbol{u}p} + (\gamma-1)\widehat{p\nabla\cdot\boldsymbol{u}} = \frac{(\gamma-1)}{Re}\widehat{\boldsymbol{\sigma}:\boldsymbol{S}} + i\boldsymbol{k}\cdot\frac{1}{M_\infty^2 PrRe}\widehat{\mu(T)\nabla T} + i\boldsymbol{k}\cdot\frac{1}{\gamma M_\infty^2}\frac{C_0}{Pr_t}h^2\widehat{|\boldsymbol{S}^h|\nabla T^h} \tag{23}$$

where the hat denotes the Fourier coefficient of a variable corresponding to a wavenumber $\boldsymbol{k}$. In addition $\rho = \rho^h + \rho'$, $\boldsymbol{m} = \boldsymbol{m}^h + \boldsymbol{m}'$, $p = p^h + p'$, $\boldsymbol{u} = \frac{\boldsymbol{m}}{\rho}$, $\boldsymbol{u}^h = \frac{\boldsymbol{m}^h}{\rho^h}$, $T = \frac{\gamma M_\infty^2 p}{\rho}$, $T^h = \frac{\gamma M_\infty^2 p^h}{\rho^h}$, $\boldsymbol{S}$ and $\boldsymbol{S}^h$ are the symmetric gradients of $\boldsymbol{u}$ and $\boldsymbol{u}^h$ respectively, and $\boldsymbol{\sigma} = \mu(T)\boldsymbol{S}_{dev}$.

The unresolved scales are approximated by (15). In this relation $\mathbb{P}' = \mathbb{P}'^T$ is the sharp cutoff filter in wavenumber space. As a result the contribution from all terms that are linear in density, momentum and pressure is eliminated and $\boldsymbol{U}' = [\rho', \boldsymbol{m}, p']^T$ are given by

$$\rho' = 0 \tag{24}$$

$$\boldsymbol{m}' = -\mathbb{P}'\tau_m\mathbb{P}'\Big(\nabla\cdot\big(\frac{\boldsymbol{m}^h\otimes\boldsymbol{m}^h}{\rho^h}\big) - \frac{1}{Re}\nabla\cdot\boldsymbol{\sigma}^h\Big) \tag{25}$$

$$p' = -\mathbb{P}'\tau_e\mathbb{P}'\Big(\nabla\cdot(\boldsymbol{u}^h p^h) - (\gamma-1)p^h\nabla\cdot\boldsymbol{u}^h - \frac{(\gamma-1)}{Re}\Phi^h - \frac{1}{M_\infty^2 PrRe}\nabla\cdot(\mu^h\nabla T^h)\Big) \tag{26}$$

In writing the expression for the unresolved variables above we assumed a diagonal form for the matrix $\boldsymbol{\tau}$, that is $\boldsymbol{\tau} = diag(\tau_c, \tau_m, \tau_m, \tau_m, \tau_e)$. Each of τ_c, τ_m and τ_e repre-

sents a combination of an advective and a diffusive time-scale associated with differential operator for the fine scales. Our definition for $\boldsymbol{\tau}$ for the compressible Navier-Stokes equations is motivated by the work of [2, 34]. The τ's are given by

$$\begin{aligned}
\tau_c &= \frac{1}{2}\Big[\quad (\lambda^e)^2 \quad \Big]^{-1/2} \\
\tau_m &= \frac{1}{2}\Big[\quad (\lambda^e)^2 + \left(\frac{4}{h^2}\frac{<\mu^h>}{<\rho^h> Re}\right)^2 \quad \Big]^{-1/2} \\
\tau_e &= \frac{1}{2}\Big[\quad (\lambda^e)^2 + \left(\frac{4}{h^2}\frac{\gamma <\mu^h>}{<\rho^h> P_r Re}\right)^2 \quad \Big]^{-1/2}
\end{aligned} \tag{27}$$

with

$$\begin{aligned}
\frac{1}{\lambda^e} &= \frac{1-e^{-Ma}}{\lambda_1^e} + \frac{e^{-Ma}}{\lambda_2^e} \\
(\lambda_1^e)^2 &= \frac{4}{h^2} < |\boldsymbol{u}^h|^2 > (1 + 2Ma^{-2} + Ma^{-1}\sqrt{4 + Ma^{-2}}) \\
(\lambda_2^e)^2 &= \frac{4}{h^2} < |\boldsymbol{u}^h|^2 >
\end{aligned} \tag{28}$$

where $h = \frac{\pi}{k^h}$ is the grid size, $< \cdot >$ denotes the spatial average of a quantity, $Ma = \sqrt{< |\boldsymbol{u}^h|^2 >}/ < c^h >$ is the turbulent Mach number, and c^h is the speed of sound. In the equation above λ_e is the reciprocal of the characteristic advective time scale. It is a combination of a time scale that is appropriate for the low-Mach number limit (λ_2^e) and another that is appropriate for the high Mach number limit, λ_1^e. In this case λ_e can be thought of as a doubly-asymptotic approximation of the two. We note that a similar approximation was proposed in [34], however it underestimated the value of λ_e in the compressible limit.

5 Numerical Results

In this section we present results using the RBVM, the mixed RBVM and the dynamic Smagorinsky-Yoshizawa-eddy diffusivity (DSYE) model with a spectral basis. All variables are represented using a Fourier basis with a cut-off wave number denoted by k^h. The test problem corresponds to a DNS simulation of the decay of homogeneous turbulence for a compressible fluid computed in [14]. In particular we focus on the D9 case described in that paper with $\Omega =]0, 2\pi[^3$. In order to validate our implementation of the compressible Navier-Stokes equations we compute our own DNS results and compare with the results presented in [14] and achieve good agreement. The physical parameters associated with the cases we have considered are listed in Table 2. They include the initial spectrum for the turbulent kinetic energy $E(k, 0)$, the initial total kinetic energy $\frac{q^2}{2}$, the free stream Mach number M_∞, the turbulent Mach number, Ma, the Reynolds number R_e and the ratio of initial compressible to total kinetic energy χ.

For compressible flows the velocity field is comprised of solenoidal (incompressible) and dilatational (compressible) components, $\boldsymbol{u}^s$ and $\boldsymbol{u}^c$ respectively. For the case of isotropic turbulence in Fourier space the Helmholtz decomposition is unique and is given by

$$\widehat{\boldsymbol{u}}^c = [(\boldsymbol{k} \cdot \widehat{\boldsymbol{u}})/k^2]\boldsymbol{k} \tag{29}$$

$$\widehat{\boldsymbol{u}}^s = \widehat{\boldsymbol{u}} - \widehat{\boldsymbol{u}}^c \, . \tag{30}$$

Let K^s and K^c denote the turbulent kinetic energy from the solenoidal and dilatational velocity components, respectively. We define $\chi = K^c/(K^c + K^s)$ as the ratio of

Table 2: Parameters for the decay of homogeneous compressible turbulence.

$E(k,0)$	$\frac{q^2}{2}$	M_∞	Ma	Re	χ
$0.011k^4e^{-2\left(\frac{k}{4}\right)^2}$	1.3235	0.184 -0.430	0.300-0.700	376	0.2-0.6

compressible kinetic energy to the total kinetic energy.

The turbulent Mach number $Ma = \sqrt{< |\boldsymbol{u}^h|^2 >}/ < c^h >$, where $< \cdot >$ represents the spatial average and c is the local speed of sound. We approximate the turbulent Mach number with the root-mean-square Mach number $Ma \approx \sqrt{< |\boldsymbol{u}^h|^2 > /c^{h2}}$, which is easier to evaluate.

We assume that there are no fluctuations in the initial values of the thermodynamic quantities, namely pressure, density and the temperature. We choose Prandtl number $Pr = 0.7$ and the adiabatic index for air to be $\gamma = 1.4$.

These parameters lead to the development of local, weak shocks, referred to as shocklets close to the regions where the local Mach number exceeds unity. As pointed out in [14] this happens when $\nabla \cdot \boldsymbol{u}$ obtains a large negative value corresponding to the deceleration of a supersonic flow to a subsonic flow. During the decay of turbulence the local Mach number varies in the range $Ma \sim 0.1 - 0.7$, and the Taylor microscale Reynolds number, $Re_\lambda = \mathcal{O}(27 - 65)$

We solve the Navier Stokes equations on a grid with N^3 points and compute all integrals on a $(3N/2)^3$ grid. We note that even for the DNS simulation this does not de-alias all the terms, but does guarantee the accurate computation of predominantly quadratic terms. For the DNS simulation $N = 256$ and for the LES simulations $N = 32$.

For the LES calculations we use the truncated velocity field obtained from the DNS at $t/T_e = 1.2$, where $T_e = 0.667$ is the eddy turn-over time [14], as the initial condition. We compare the performance of the models from $t/T_e = 1.2 \sim 7.0$, which corresponds to a Taylor micro-scale Reynolds number of $Re_\lambda = 65.5 \sim 27.4$. For time integration we use the fourth-order Runge-Kutta algorithm, and we evaluate all terms explicitly. The details of the numerical algorithm can be found in [35].

5.1 LES with $k^h = 16$, $Ma = 0.488$, $\chi = 0.4$

Figures 1 and 2 show the turbulent kinetic energy in the incompressible and compressible velocity components, respectively, as a function of time. We observe that the no model case over-predicts these quantities. In Figure 1, for the incompressible turbulent kinetic energy, the RBVM model is most accurate followed by the mixed model, followed by the DSYE model which is clearly too dissipative. The RBVM model slightly over-predicts the kinetic energy while the mixed model under-predicts it. The evolution of the compressible component of the kinetic energy is shown in Figure 2 and all three LES models perform well. Here the mixed model is the most accurate followed closely by the RBVM model, which slightly over-predicts the kinetic energy. The DSYE model is once again overly dissipative.

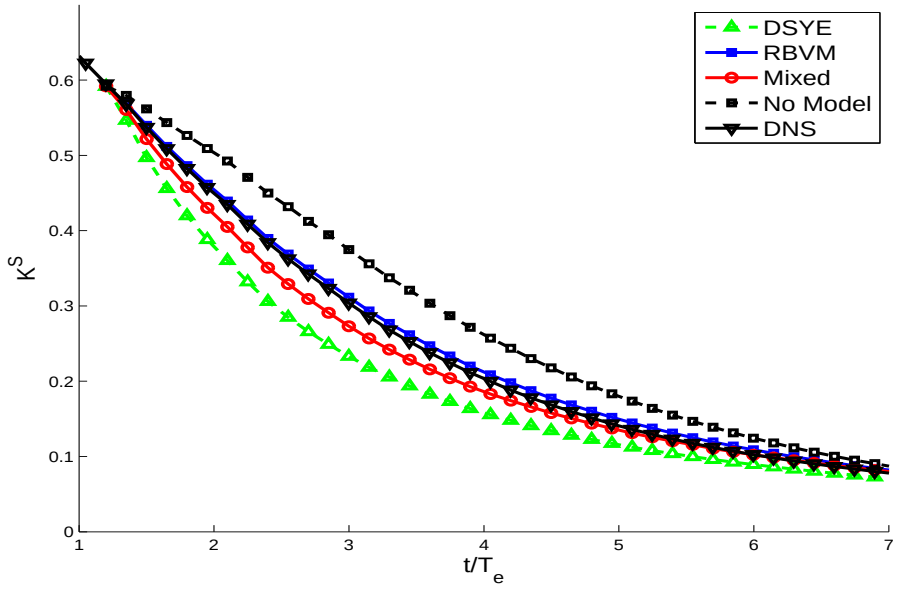

Figure 1: Evolution of turbulent kinetic energy of the incompressible velocity component for $k^h = 16$, $\chi = 0.4$, $Ma = 0.488$.

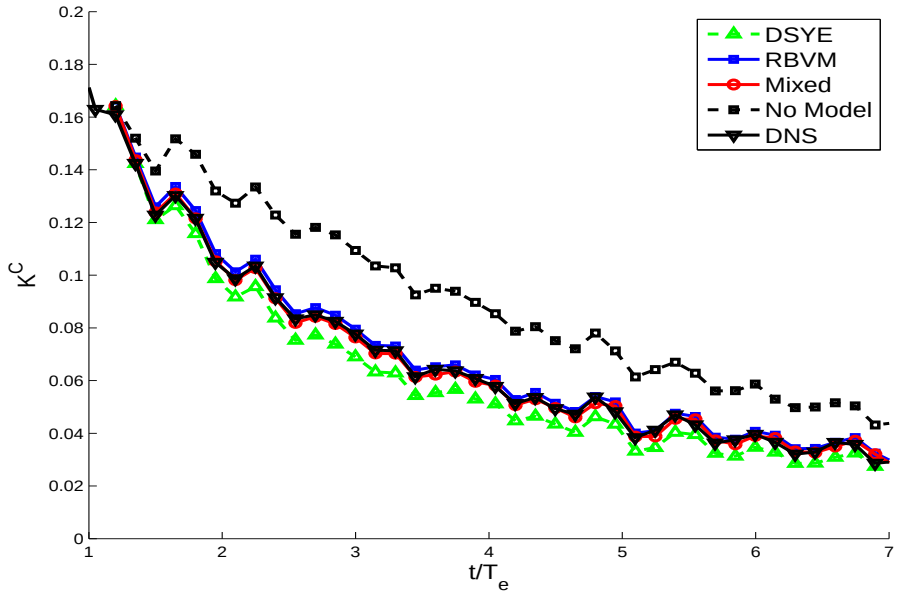

Figure 2: Evolution of turbulent kinetic energy of the compressible velocity component for $k^h = 16$, $\chi = 0.4$, $Ma = 0.488$.

This behavior is explained by examining the incompressible and compressible energy spectra at $t/T_e \approx 3.0$ in Figures 3 and 4 and at $t/T_e \approx 6.0$ in Figures 5 and 6.

From the figure for the incompressible spectra at $t/T_e \approx 3.0$ (Figure 3) we observe that the no-model case displays a pile-up of energy at high wavenumbers. All the LES models are quite accurate at low-to-mid wavenumbers, while the RBVM is the most accurate at high wavenumbers, followed by the mixed model. At $t/T_e \approx 6.0$ (Figure 5) the mixed model is the most accurate at the mid-to-high wavenumbers whereas the RBVM model is most accurate at low wavenumbers. In either case the DSYE model is the least accurate.

For the compressible spectra in Figures 4 and 6 we observe that the energy pile-up in the no-model case is not as large as in the incompressible case thereby indicating that the compressible component of the subgrid model plays a smaller role. All the LES models appear to perform quite well with the RBVM and the mixed models being the most accurate at high wavenumbers. The same conclusions can be drawn for the density and pressure spectra at time $t/T_e \approx 6.0$, shown in Figures 7 and 8, respectively. The evolution of the root-mean-square (rms) density is shown in Figure 9. Once again the DSYE model is observed to lead to smaller rms values while the RBVM and the mixed model are more accurate.

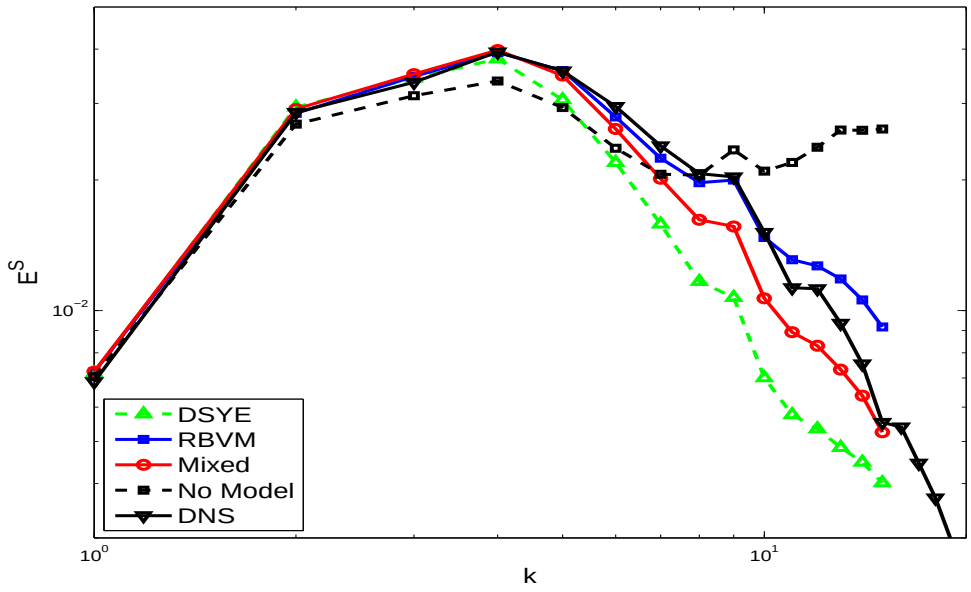

Figure 3: Energy spectrum of the incompressible velocity component for $k^h = 16$, at $t/T_e \approx 3$, $\chi = 0.4$, $Ma = 0.488$.

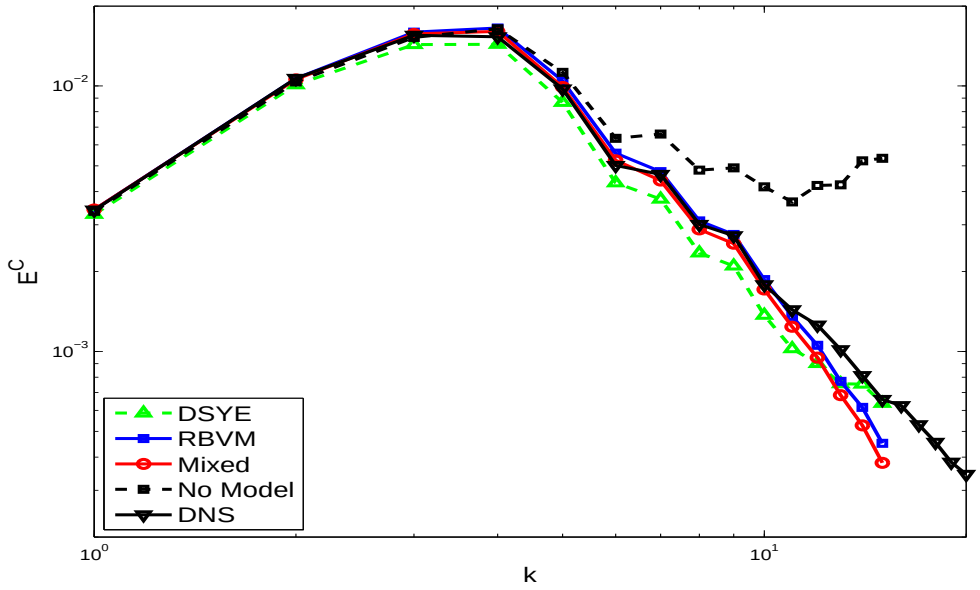

Figure 4: Energy spectrum of the compressible velocity component for $k^h = 16$, at $t/T_e \approx 3$, $\chi = 0.4$, $Ma = 0.488$.

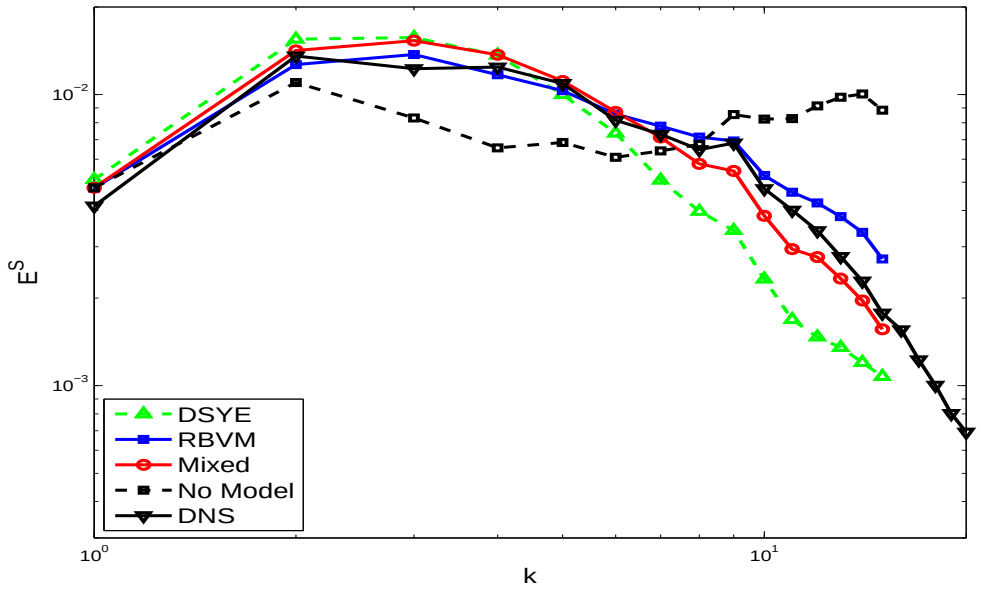

Figure 5: Energy spectrum of the incompressible velocity component for $k^h = 16$, at $t/T_e \approx 6$, $\chi = 0.4$, $Ma = 0.488$.

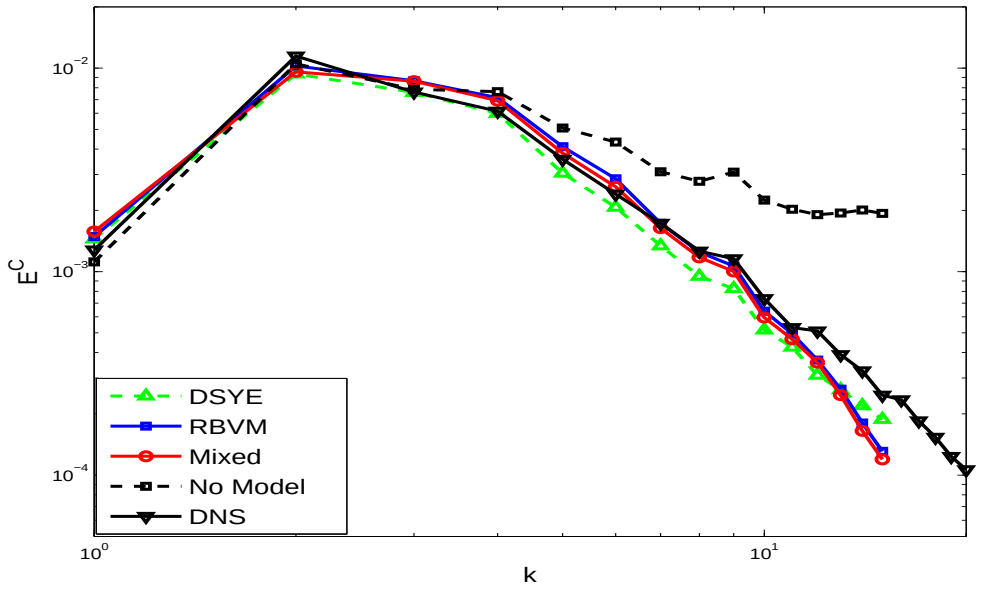

Figure 6: Energy spectrum of the compressible velocity component for $k^h = 16$, at $t/T_e \approx 6$, $\chi = 0.4$, $Ma = 0.488$.

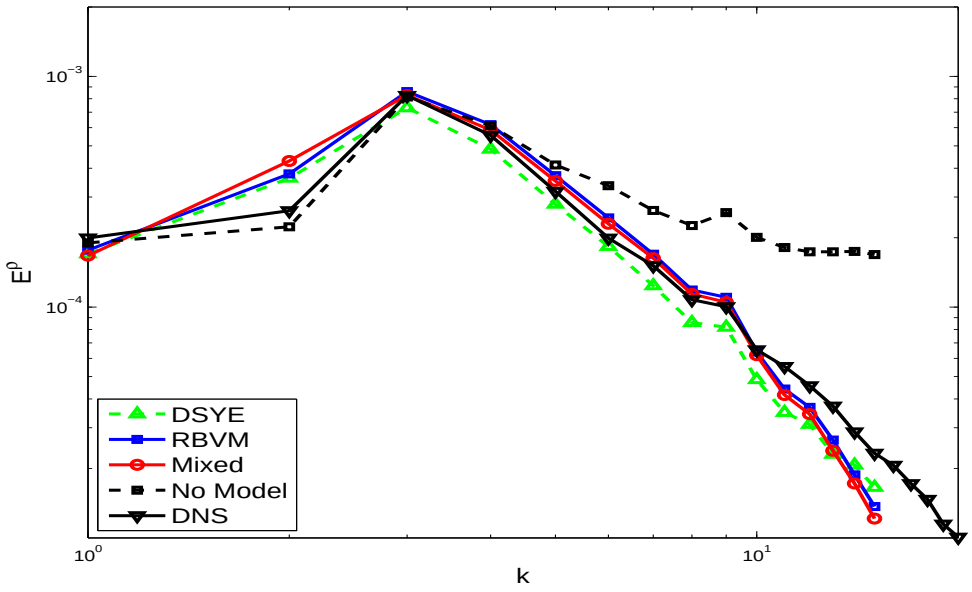

Figure 7: Density spectrum of for $k^h = 16$, at $t/T_e \approx 6.0$, $\chi = 0.4$, $Ma = 0.488$.

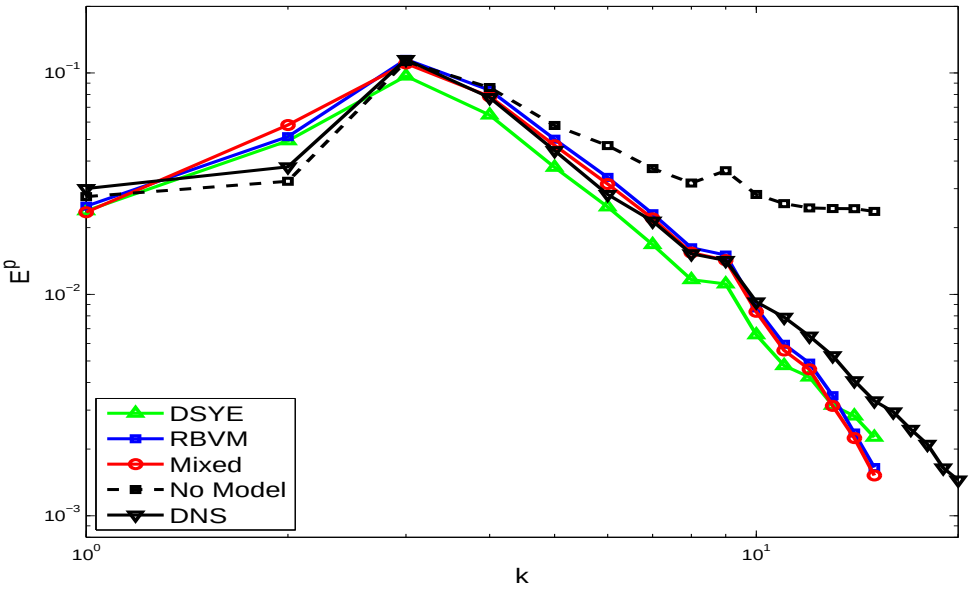

Figure 8: Pressure spectrum of for $k^h = 16$, at $t/T_e \approx 6.0$, $\chi = 0.4$, $Ma = 0.488$.

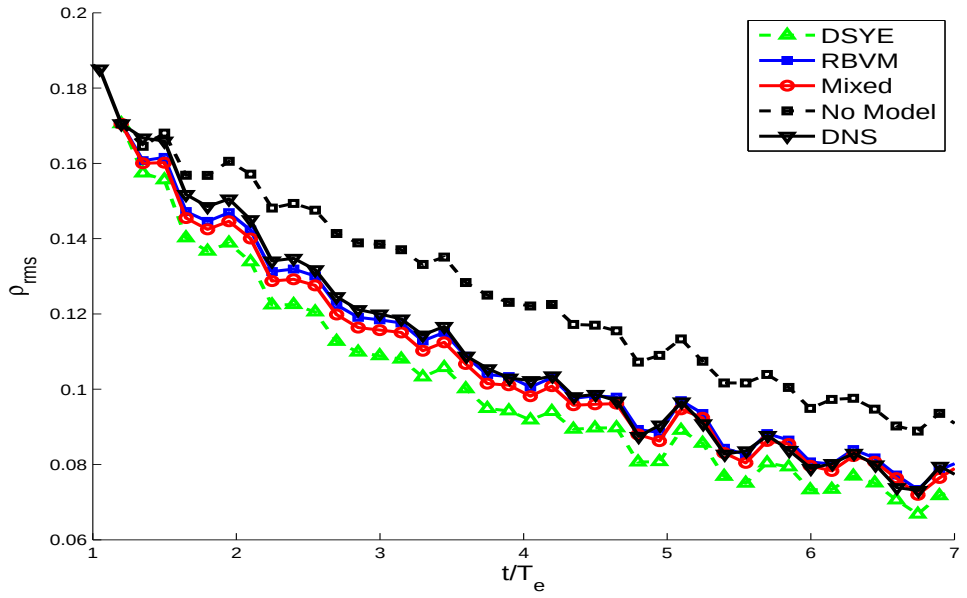

Figure 9: Evolution of density rms for $k^h = 16$, $\chi = 0.4$, $Ma = 0.488$.

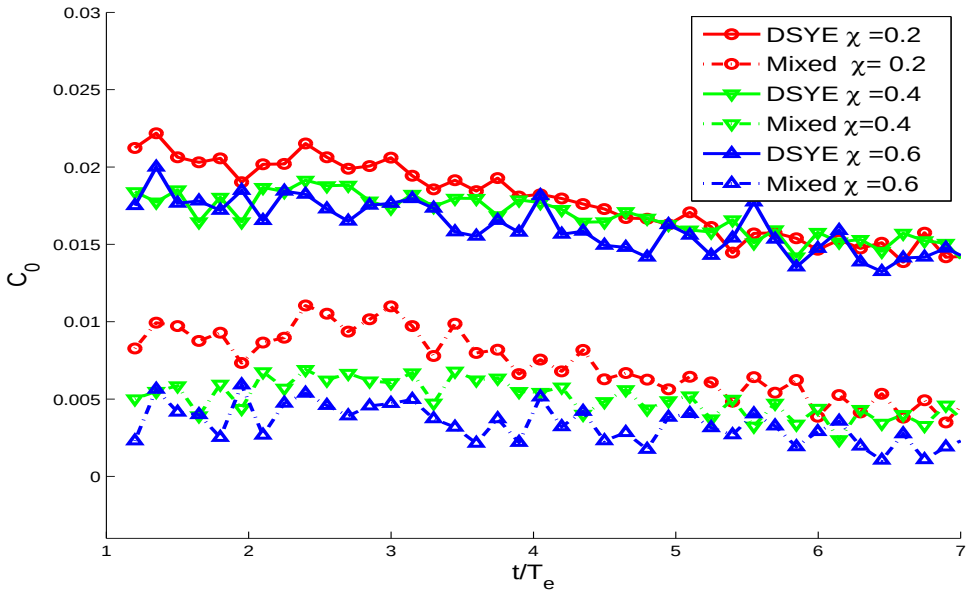

Figure 10: Evolution of the Smagorinsky coefficient C_0 for the dynamic Smagorinsky and the mixed model for $k^h = 16$, $Ma = 0.488$.

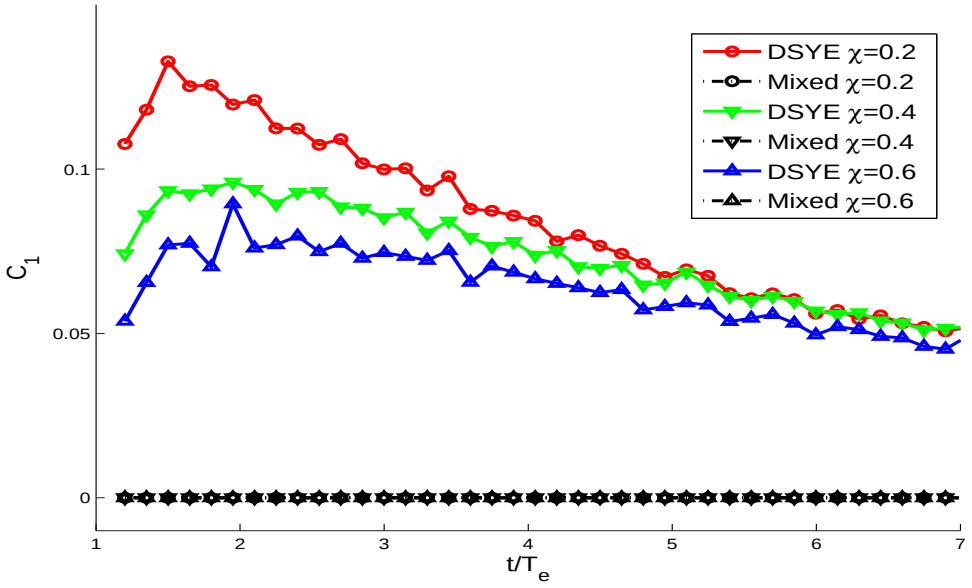

Figure 11: Evolution of the Smagorinsky coefficient C_1 the mixed model for $k^h = 16$, $Ma = 0.488$.

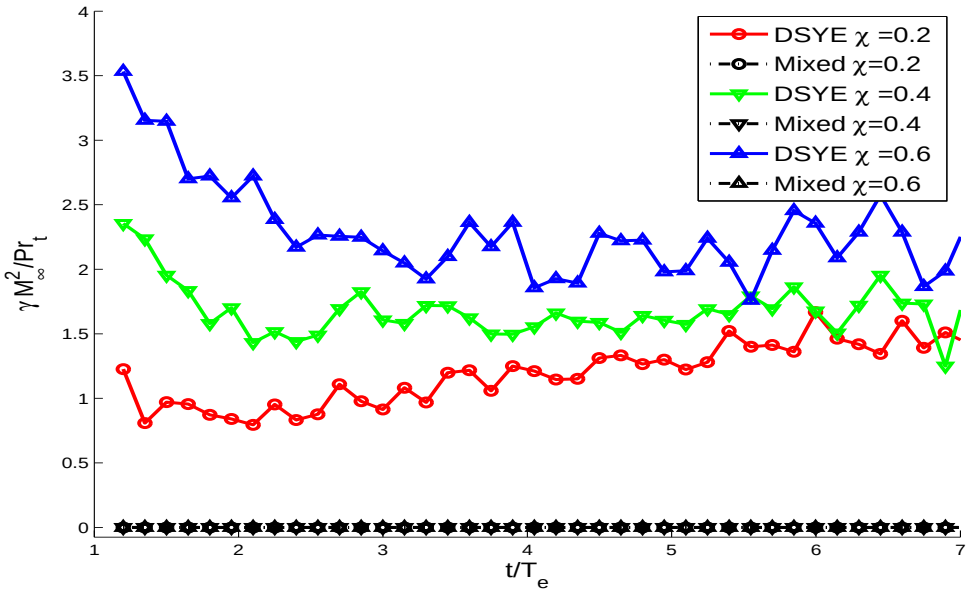

Figure 12: Evolution of Pr_t for the dynamic Smagorinsky model for $k^h = 16$, $Ma = 0.488$.

We have also performed these simulations with $k^h = 32$ (not shown here). We observe the same trends however the differences between all the models are much smaller.

5.2 Effect of varying χ

In this section we examine the effect of varying the initial fraction of the compressible turbulent kinetic energy. In particular we select $\chi = 0.2$ and $\chi = 0.6$ to add to the $\chi = 0.4$ case described in the previous section. The Mach number $Ma = 0.488$ is unchanged.

When χ is small a greater proportion of the total initial kinetic energy is incompressible. As a result a larger contribution from the deviatoric component of the subgrid stress is required. The dynamic Smagorinsky and mixed models respond to this by increasing the value of the model parameters with decreasing values of χ. This is seen in Figure 10, where we have plotted value of the deviatoric parameter C_0 as a function of time. We observe that with increasing time all parameters tend to smaller values because of the natural decay in the turbulence intensity. We also note that the value of C_0 for the mixed model is consistently smaller than the dynamic Smagorinsky model, indicating that the dynamic procedure is accounting for the additional dissipation generated by the RBVM component of the mixed model. With increasing value of χ the ratio of the average value of C_0 for the mixed model to the corresponding value for the dynamic Smagorinsky model appears to decreasing, indicating that for large values of χ the mixed model is tending toward the RBVM model.

For completeness the variation of the other dynamic parameters that is C_1 and Pr_t^{-1}

as a function of time is shown in Figures 11 and 12, respectively. The value of C_1 in the mixed model is selected to be zero as discussed in Section 3. The value of Pr_t^{-1} for the mixed model is also zero because the dynamic procedure yields a negative value which is ignored.

In Figure 13 we have plotted the spectrum for the incompressible velocity component for different models for $\chi = 0.2$ and $t/T_e \approx 6$. We note that RBVM model is the most accurate for low wavenumbers whereas the mixed model is the most accurate for high wavenumbers. The DSYE model is too dissipative. The spectrum for the compressible component is shown in Figure 14. All models are very accurate for small wavenumbers whereas the RBVM and the mixed model are slightly more accurate for high wavenumbers.

In Figure 15 we have plotted the spectrum for the incompressible velocity component for different models for $\chi = 0.6$ and $t/T_e \approx 6$. We note that RBVM model is the most accurate overall followed by the mixed model. The DSYE model continues to be too dissipative. The spectrum for the compressible component is shown in Figure 16. Here all the models are very accurate for the entire range of wavenumbers.

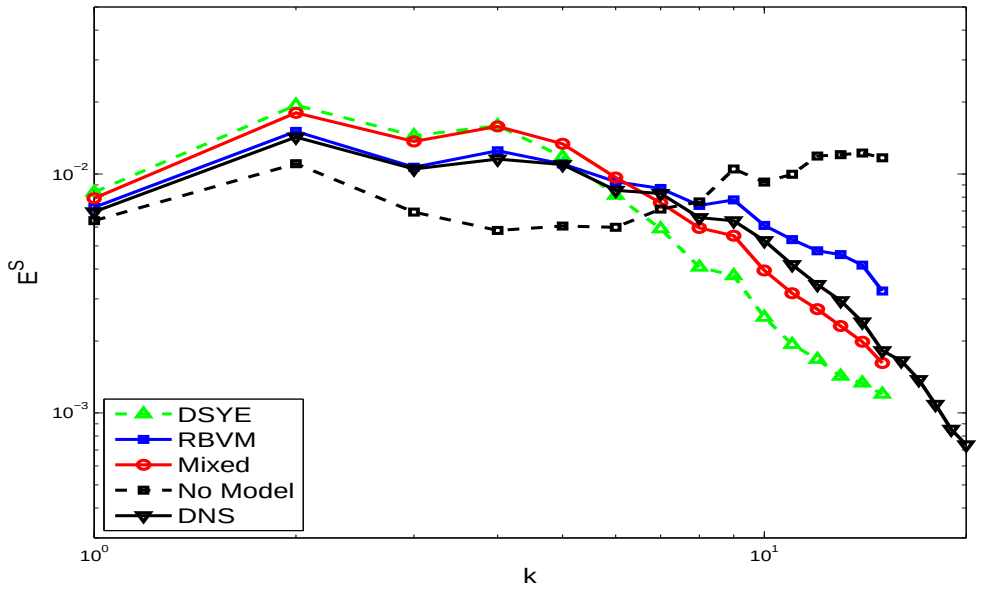

Figure 13: Energy spectrum of the incompressible velocity component for $k^h = 16$, at $t/T_e \approx 6$, $\chi = 0.2$, $Ma = 0.488$.

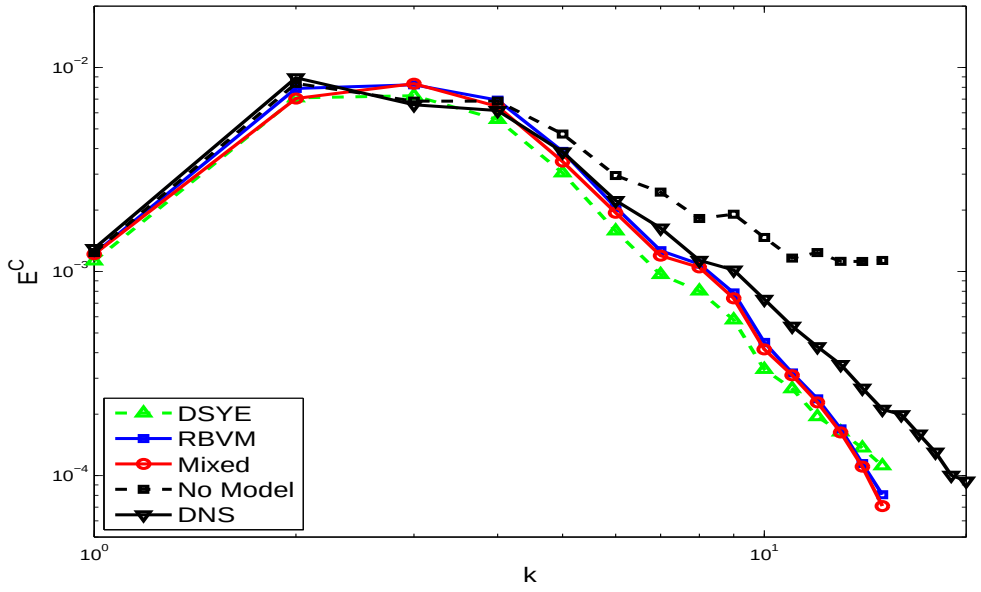

Figure 14: Energy spectrum of the compressible velocity component for $k^h = 16$, at $t/T_e \approx 6$, $\chi = 0.2$, $Ma = 0.488$.

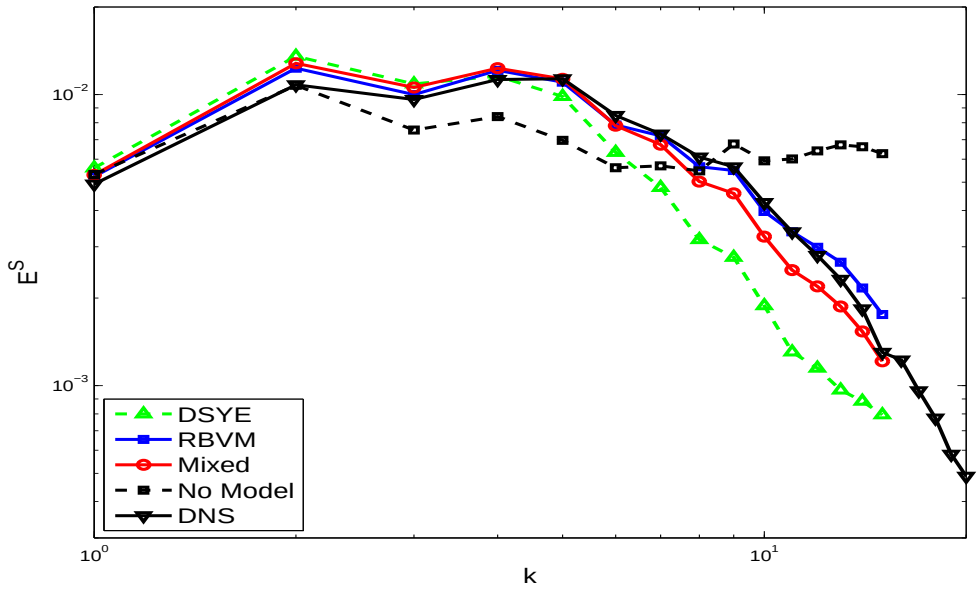

Figure 15: Energy spectrum of the incompressible velocity component for $k^h = 16$, at $t/T_e \approx 6$, $\chi = 0.6$, $Ma = 0.488$.

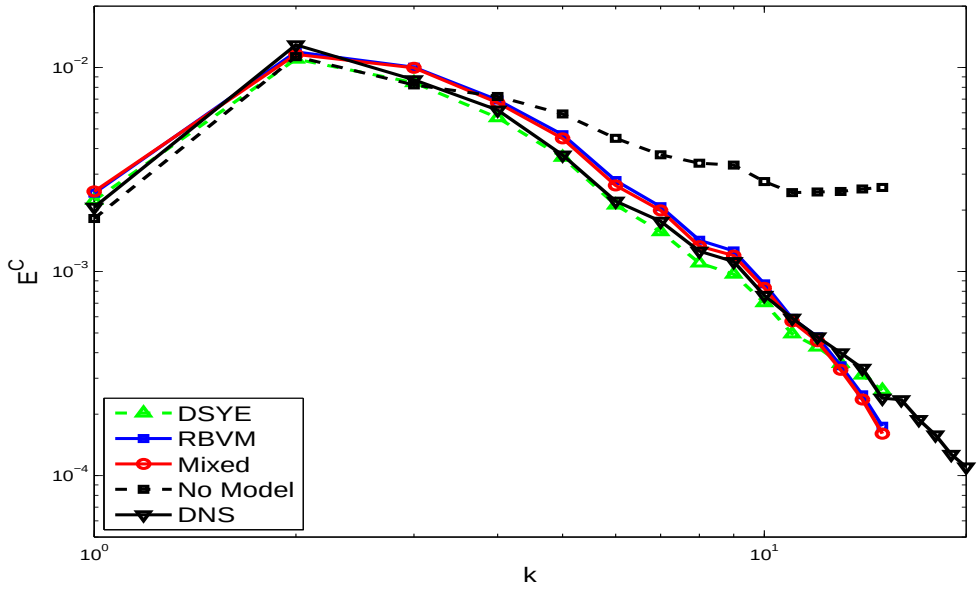

Figure 16: Energy spectrum of the compressible velocity component for $k^h = 16$, at $t/T_e \approx 6$, $\chi = 0.6$, $Ma = 0.488$.

5.3 Effect of Ma

In this section we test the robustness of the LES models with regards to the inherent compressibility of the flow by varying the Mach number. In addition to $Ma = 0.488$, which was considered in Section 5.1, we consider $Ma = 0.3$ and $Ma = 0.7$, while fixing $\chi = 0.4$.

In Figure 17 we have plotted the spectrum of the incompressible component of the velocity at $t/T_e \approx 6$ for $Ma = 0.3$. At this value of Ma the flow is nearly incompressible. We note that the RBVM and the mixed model are very close to each other and to the exact solution while the DSYE model is inaccurate. In Figure 21 we have plotted the variation of the deviatoric parameter C_0, as computed by the dynamic procedure, as a function of time. We observe that for $Ma = 0.3$ this parameter is very small indicating that the mixed model is essentially the same as the RBVM model.

From the plot of the spectrum of the compressible component of kinetic energy at $t/T_e \approx 6$ (see Figure 18) we conclude that all the LES models are quite accurate.

In Figure 19 we have plotted the spectrum of the incompressible component of the velocity at $t/T_e \approx 6$ for $Ma = 0.7$. At this high Mach number we expect the compressible effects to be more pronounced and we would also expect the formation relatively strong local shocks. From the plot we observe that the RBVM model is most accurate in this case followed by the mixed model. The latter is somewhere between the RBVM and the DSYE model. This may be understood by observing the variation of C_0 for these two models with time (see Figure 21). We note that the value of C_0 for

the mixed model is higher than it was for $Ma = 0.3$, indicating that its performance will be closer to that of the DSYE model in this case.

From the plot of the spectrum of the compressible component of the velocity we observe that the RBVM and the mixed models are very accurate while the DSYE model underestimates the spectrum.

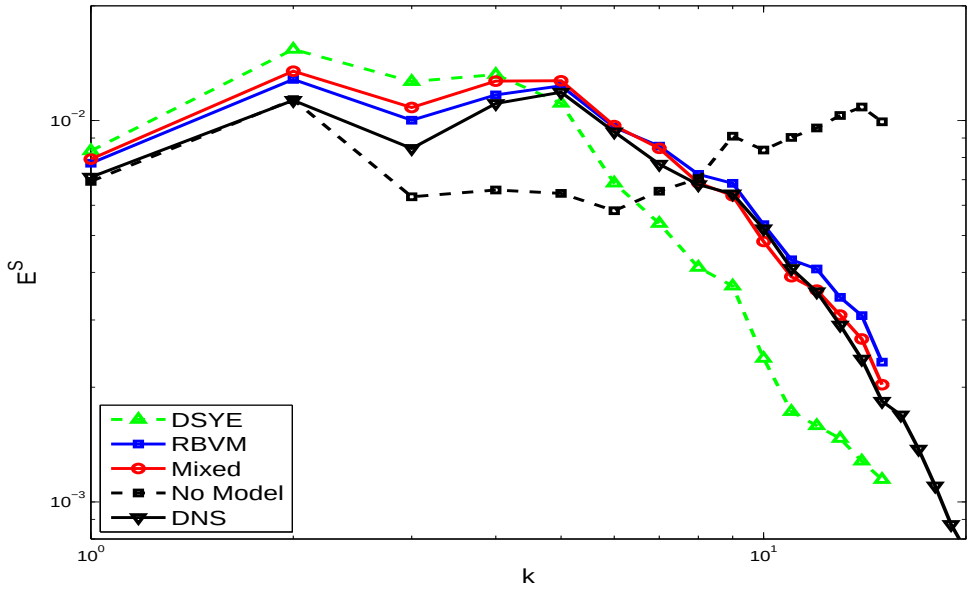

Figure 17: Energy spectrum of the incompressible velocity component for $k^h = 16$, at $t/T_e \approx 6$, $\chi = 0.4$, $Ma = 0.300$.

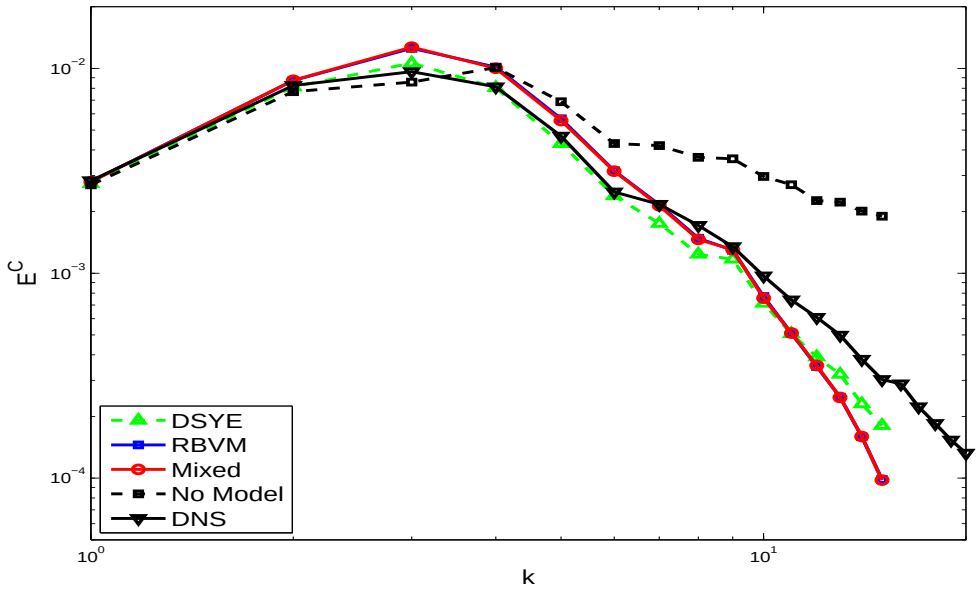

Figure 18: Energy spectrum of the compressible velocity component for $k^h = 16$, at $t/T_e \approx 6$, $\chi = 0.4$, $Ma = 0.300$.

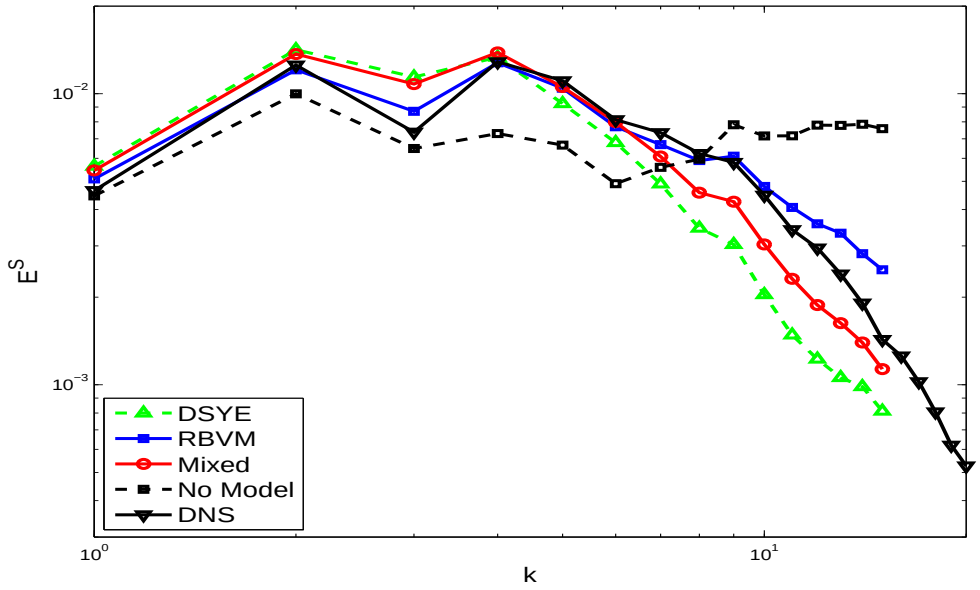

Figure 19: Energy spectrum of the incompressible velocity component for $k^h = 16$, at $t/T_e \approx 6$, $\chi = 0.4$, $Ma = 0.700$.

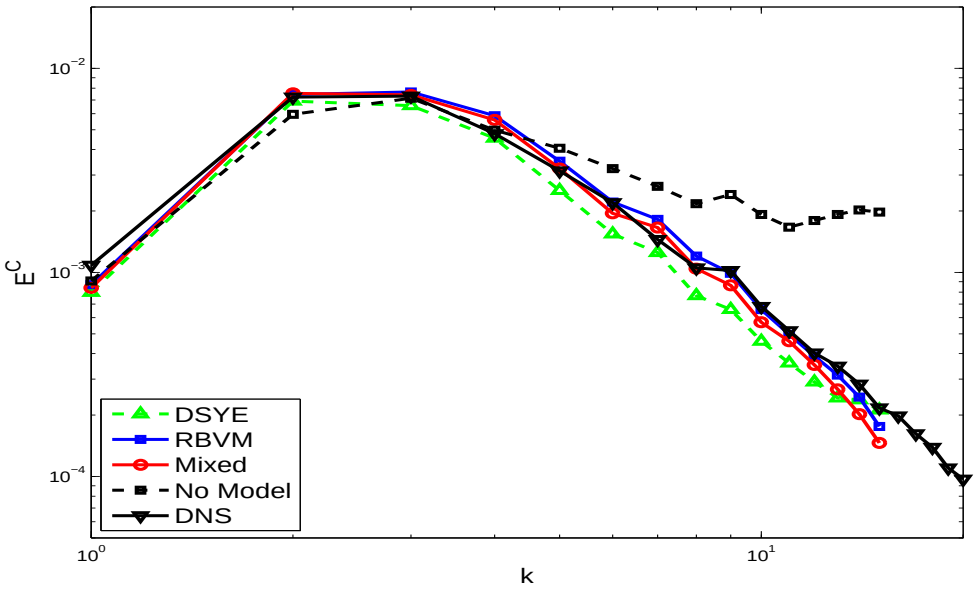

Figure 20: Energy spectrum of the compressible velocity component for $k^h = 16$, at $t/T_e \approx 6$, $\chi = 0.4$, $Ma = 0.700$.

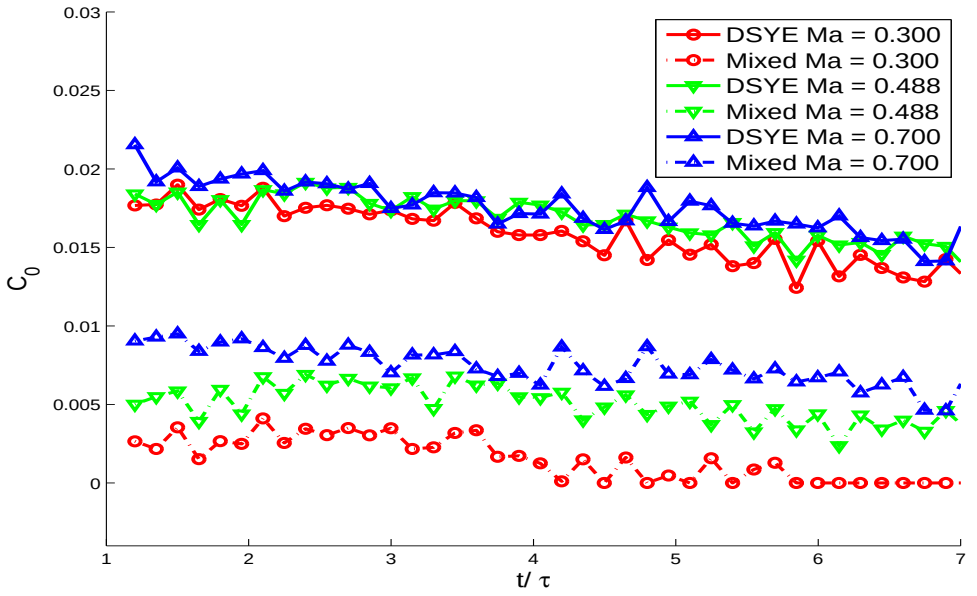

Figure 21: Comparison of the Smagorinsky coefficient C_0 for the dynamic Smagorinsky and the mixed model for $k^h = 16$, $\chi = 0.4$.

5.4 High Reynolds number

In this section the performance of the LES models at a higher Reynolds number is considered. The DNS was computed using 512^3 modes ($k^h = 256$) in and all other parameters were the same as for the previous run, except the Reynolds number which was set to $Re = 843$. In addition, $\chi = 0.4$ and $Ma = 0.488$ were chosen. For the LES models, which were performed with 32^3 modes ($k^h = 16$), we used the truncated velocity field obtained from the DNS at $t/T_e = 0.92$ as initial condition, where $T_e = 0.667$ is the eddy turn-over time. We compare the performance of the models in the interval $t/T_e = 0.92 - 7.0$, which corresponds to a Taylor micro-scale Reynolds number of $Re_\lambda = 120.95 - 41.97$. For the RBVM and the mixed model, Fourier modes with $k \in (16, 24)$ were used to compute the approximate fine scales.

In Figures 22-25, we have plotted the Energy spectrum of the incompressible and compressible velocity component at time $t/T_e \approx 3$ and $t/T_e \approx 6$. Once again, for incompressible velocity component, we observe that the DSYE model is too dissipative. However, the RBVM here is not dissipative enough, and the mixed model is the most accurate, especially at time $t/T_e \approx 6$ in Figure 23. In Figure 22 and 25, for the compressible velocity component, all the LES models are equally accurate; the DSYE model is slightly dissipative in the middle wavenumber range.

In the examples presented in the previous section, the Reynolds number of the flow was moderate. As a result the cross-stress term was the dominant term, and since the RBVM model captured this term well there was little or no benefit in including the

Reynolds stress term via the Smagorinsky model. However, after performing this test at a higher Reynolds number, we can observe the benefit of using the mixed model.

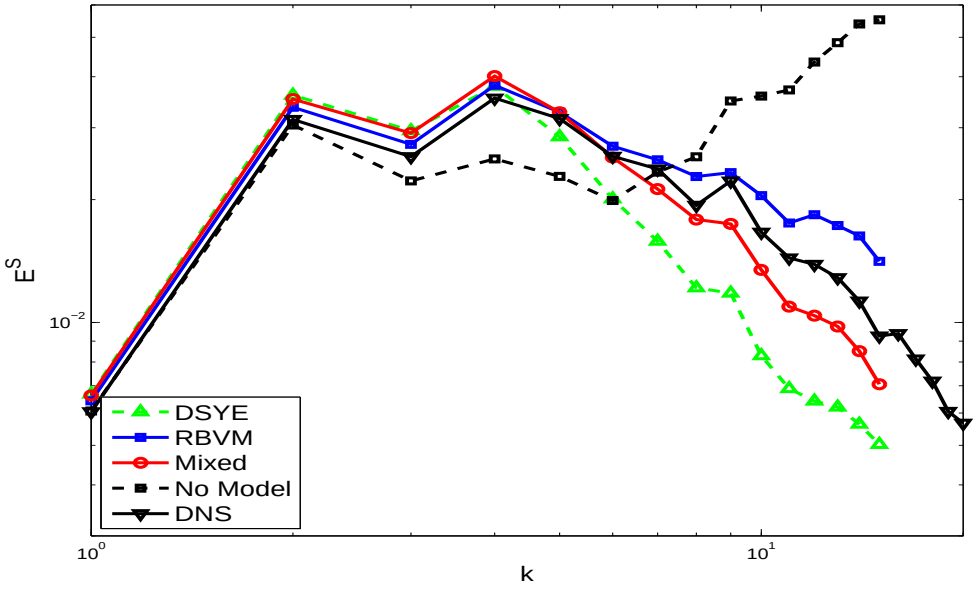

Figure 22: Energy spectrum of the incompressible velocity component for $k^h = 16$, at $t/T_e \approx 3$, $\chi = 0.4$, $Ma = 0.488$.

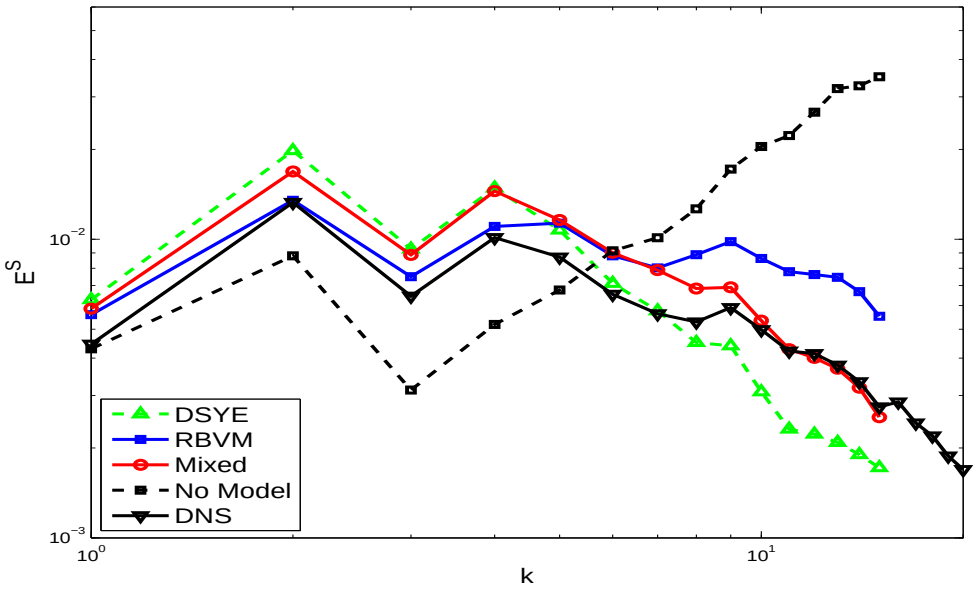

Figure 23: Energy spectrum of the incompressible velocity component for $k^h = 16$, at $t/T_e \approx 6$, $\chi = 0.4$, $Ma = 0.488$.

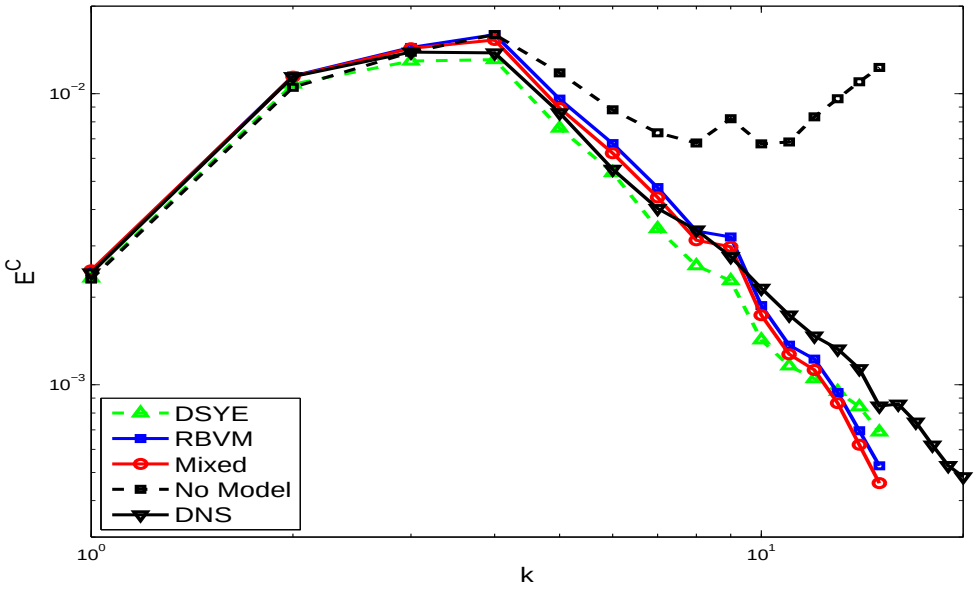

Figure 24: Energy spectrum of the compressible velocity component for $k^h = 16$, at $t/T_e \approx 3$, $\chi = 0.4$, $Ma = 0.488$.

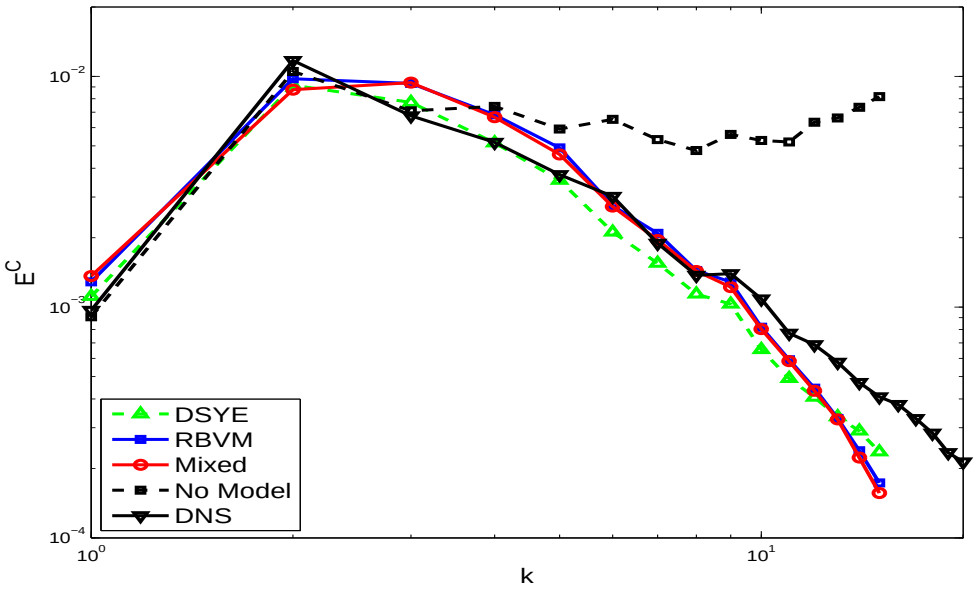

Figure 25: Energy spectrum of the compressible velocity component for $k^h = 16$, at $t/T_e \approx 6$, $\chi = 0.4$, $Ma = 0.488$.

6 Conclusions

We have developed and implemented the residual-based variational multiscale (RBVM) model for compressible turbulent flows. Motivated by earlier results for incompressible flows we have also considered a mixed version of this model wherein Smagorinsky, Yoshizawa and eddy-diffusivity terms are added in order to better model the Reynolds stress contributions. Through energy analysis of the mixed model we have demonstrated that the Yoshizawa model is redundant because the RBVM model itself introduces a viable Reynolds stress term for the dilatational component of subgrid stresses. In addition, from the dynamic procedure we have found that the eddy-diffusivity term

in the energy equation is not required for the mixed RBVM model. As a result the mixed RBVM model contains only one term in addition to the RBVM model. This term models the Reynolds stress component of the deviatoric part of subgrid stresses and is represented by a Smagorinsky-type model.

We have tested the performance of the RBVM, the mixed and the dynamic Smagorinsky-Yoshizawa-eddy diffusivity (DSYE) models in predicting the decay of compressible, homogeneous, isotropic turbulence in regimes where shocklets are known to exist. We have varied the level of compressibility of the flow by varying the initial proportion of turbulent kinetic energy and by varying the Mach number. In all cases we have found that RBVM and the mixed models are equally accurate and perform significantly better than the DSYE model. We have also found that for the mixed model the variational counterpart of the Germano identity automatically accounts for the dissipation produced by the RBVM terms and produces smaller Smagorinsky parameter when compared to the dynamic Smagorinsky model.

Acknowledgments

The support of NSF Grant CTS-0449151 is gratefully acknowledged. Also the support of the Center for Computational Nanotechnology Innovations (CCNI) and the SUR Blue Gene at Rensselaer Polytechnic Institute for the DNS calculation is acknowledged. The senior author would like to acknowledge support of Erasmus Mundus Master Course Lectureship at Universidad Politécnica de Cataluña and the Humboldt Foundation

award for experienced researchers.

Appendix A: Derivation of the dynamic calculation for C_0, C_1 and Pr_t.

In this section we describe the dynamic procedure we have used to determine the unknown parameters in the LES models. We have utilized the variational counterpart of the Germano identity described in [29, 30].

DSYE model

The equations for this model are given by (17) with $\boldsymbol{U}' = 0$. In this equation, in order to focus on the momentum equations we select $\boldsymbol{W}^h = [0, \boldsymbol{w}^h, 0]$, to arrive at

$$\begin{aligned}(\boldsymbol{w}^h, \boldsymbol{m}^h_{,t}) - (\nabla \boldsymbol{w}^h, \frac{\boldsymbol{m}^h \otimes \boldsymbol{m}^h}{\rho^h}) - (\nabla \cdot \boldsymbol{w}^h, p^h) + \frac{1}{Re}(\nabla \boldsymbol{w}^h, \boldsymbol{\sigma}^h) \\ + \left(\nabla \boldsymbol{w}^h, 2C_0 \rho^h h^2 |\boldsymbol{S}^h| \boldsymbol{S}^h_{dev} - \frac{2}{3} C_1 \rho^h h^2 |\boldsymbol{S}^h|^2 \boldsymbol{I} \right) = 0, \qquad \forall \boldsymbol{w}^h.\end{aligned} \tag{31}$$

In the equations above $h = \pi/k^h$, where k^h is the cutoff wavenumber. The equations for the same model used in a coarser discretization with the finite dimensional space $\mathcal{V}^H \subset \mathcal{V}^h$ are given by

$$\begin{aligned}(\boldsymbol{w}^H, \boldsymbol{m}^H_{,t}) - (\nabla \boldsymbol{w}^H, \frac{\boldsymbol{m}^H \otimes \boldsymbol{m}^H}{\rho^H}) - (\nabla \cdot \boldsymbol{w}^H, p^H) + \frac{1}{Re}(\nabla \boldsymbol{w}^H, \boldsymbol{\sigma}^H) \\ + \left(\nabla \boldsymbol{w}^H, 2C_0 \rho^H H^2 |\boldsymbol{S}^H| \boldsymbol{S}^H_{dev} - \frac{2}{3} C_1 \rho^H H^2 |\boldsymbol{S}^H|^2 \boldsymbol{I} \right) = 0 \qquad \forall \boldsymbol{w}^H,\end{aligned} \tag{32}$$

where $H = \pi/k^H$, where k^H is the cutoff wavenumber at the H-scale. In this study we

have selected $k^H = k^h/2$. Since $\mathcal{V}^H \subset \mathcal{V}^h$, we replace $\boldsymbol{w}^h$ with $\boldsymbol{w}^H$ in (31), and subtract the resulting equation from (32) to arrive at

$$\begin{aligned}
&\left(\nabla \boldsymbol{w}^H, \frac{\boldsymbol{m}^h \otimes \boldsymbol{m}^h}{\rho^h} - \frac{\boldsymbol{m}^H \otimes \boldsymbol{m}^H}{\rho^H}\right) = \\
&-2C_0\left(\nabla \boldsymbol{w}^H, \rho^H H^2 |\boldsymbol{S}^H| \boldsymbol{S}^h_{dev} - \rho^h h^2 |\boldsymbol{S}^h| \boldsymbol{S}^h_{dev}\right) \\
&+\frac{2}{3}C_1\left(\nabla \boldsymbol{w}^H, \rho^H H^2 |\boldsymbol{S}^H|^2 \boldsymbol{I} - \rho^h h^2 |\boldsymbol{S}^h|^2 \boldsymbol{I}\right), \qquad \forall \boldsymbol{w}^H.
\end{aligned} \tag{33}$$

In arriving the this equation we have set

$$\begin{aligned}
(\boldsymbol{w}^H, \boldsymbol{m}^H_{,t} - \boldsymbol{m}^h_{,t}) = 0, \\
(\nabla \cdot \boldsymbol{w}^H, p^H - p^h) = 0, \\
(\nabla \boldsymbol{w}^H, \boldsymbol{\sigma}^H - \boldsymbol{\sigma}^h) = 0,
\end{aligned} \tag{34}$$

The first two relations above hold exactly for a Fourier-spectral spatial discretization, while the last is an assumption.

In (33) we select $\nabla \boldsymbol{w}^H = \boldsymbol{S}^H_{dev}$, and recognize that $(\boldsymbol{S}_{dev}, \boldsymbol{I}) = 0$, to arrive at

$$\begin{aligned}
&\left(\boldsymbol{S}^H_{dev}, \frac{\boldsymbol{m}^h \otimes \boldsymbol{m}^h}{\rho^h} - \frac{\boldsymbol{m}^H \otimes \boldsymbol{m}^H}{\rho^H}\right) = \\
&-2C_0(\boldsymbol{S}^H_{dev}, \rho^H H^2 |\boldsymbol{S}^H| \boldsymbol{S}^H_{dev} - \rho^h h^2 |\boldsymbol{S}^h| \boldsymbol{S}^h_{dev}),
\end{aligned} \tag{35}$$

which yields the final expression for C_0,

$$C_0 = -\frac{1}{2}\frac{\left(\boldsymbol{S}^H_{dev}, \frac{\boldsymbol{m}^h \otimes \boldsymbol{m}^h}{\rho^h} - \frac{\boldsymbol{m}^H \otimes \boldsymbol{m}^H}{\rho^H}\right)}{\left(\boldsymbol{S}^H_{dev}, \rho^H H^2 |\boldsymbol{S}^H| \boldsymbol{S}^H_{dev} - \rho^h h^2 |\boldsymbol{S}^h| \boldsymbol{S}^h_{dev}\right)}. \tag{36}$$

In order to determine we select $\nabla \boldsymbol{w}^H = \boldsymbol{I}$ in (33), to arrive at to arrive at

$$\begin{aligned} &\Big(1, tr\big(\frac{\boldsymbol{m}^h \otimes \boldsymbol{m}^h}{\rho^h} - \frac{\boldsymbol{m}^H \otimes \boldsymbol{m}^H}{\rho^H}\big)\Big) = \\ &2C_1(1, \rho^H H^2 |\boldsymbol{S}^H|^2 - \rho^h h^2 |\boldsymbol{S}^h|^2), \end{aligned} \tag{37}$$

which yields

$$C_1 = \frac{1}{2} \frac{\Big(1, tr\big(\frac{\boldsymbol{m}^h \otimes \boldsymbol{m}^h}{\rho^h} - \frac{\boldsymbol{m}^H \otimes \boldsymbol{m}^H}{\rho^H}\big)\Big)}{(1, \rho^H H^2 |\boldsymbol{S}^H|^2 - \rho^h h^2 |\boldsymbol{S}^h|^2)}. \tag{38}$$

In order to determine the turbulent Prandtl number (17), we choose $\boldsymbol{W}^h = [0, 0, q^h]$ to get

$$\begin{aligned} &(q^h, p^h_{,t}) - (\nabla q^h, \boldsymbol{u}^h p^h) - (1-\gamma)(q^h, p^h \nabla \cdot \boldsymbol{u}^h) \\ &- \frac{(\gamma-1)}{Re}(q^h, \Phi^h) + \frac{1}{M^2_\infty PrRe}(\nabla q^h, \mu^h \nabla T^h) \\ &+ \big(\nabla q^h, \quad \frac{C_0}{Pr_t \gamma M^2_\infty} h^2 \rho^h |\boldsymbol{S}^h| \nabla T^h\big) = 0, \qquad \forall q^h. \end{aligned} \tag{39}$$

Similarly at the $H-$scale we arrive at

$$\begin{aligned} &(q^H, p^H_{,t}) - (\nabla q^H, \boldsymbol{u}^H p^H) - (1-\gamma)(q^H, p^H \nabla \cdot \boldsymbol{u}^H) \\ &- \frac{(\gamma-1)}{Re}(q^H, \Phi^H) + \frac{1}{M^2_\infty PrRe}(\nabla q^H, \mu^H \nabla T^H) \\ &+ \big(\nabla q^H, \quad \frac{C_0}{Pr_t \gamma M^2_\infty} H^2 \rho^H |\boldsymbol{S}^H| \nabla T^H\big) = 0, \qquad \forall q^H. \end{aligned} \tag{40}$$

Since $\mathcal{V}^H \subset \mathcal{V}^h$, we may replace q^h with q^H in (39) and subtract the result from (40) to arrive at

$$\begin{aligned} &\Big(\nabla q^H, \frac{\boldsymbol{m}^h p^h}{\rho^h} - \frac{\boldsymbol{m}^H p^H}{\rho^H}\Big) = \\ &\frac{C_0}{Pr_t \gamma M^2_\infty}\Big(\nabla q^H, h^2 \rho^h |\boldsymbol{S}^h| \nabla T^h - H^2 \rho^H |\boldsymbol{S}^H| \nabla T^H\Big), \qquad \forall q^H. \end{aligned} \tag{41}$$

Where we have made use of

$$\begin{aligned}(q^H, p^H_{,t}) - (q^H, p^h_{,t}) = 0,\\ (q^H, p^H \nabla \cdot \boldsymbol{u}^H) - (q^H, p^h \nabla \cdot \boldsymbol{u}^h) = 0,\\ (q^H, \Phi^H) - (q^H, \Phi^h) = 0,\\ (\nabla q^H, \mu^H \nabla T^H) - (\nabla q^H, \mu^h \nabla T^h) = 0.\end{aligned} \tag{42}$$

The first relation above holds exactly for a Fourier-spectral spatial discretization, while the others are assumed. We let $\nabla q^H = \nabla T^H$, in (41) and arrive at

$$\begin{aligned}\left(\nabla T^H, \frac{\boldsymbol{m}^h p^h}{\rho^h} - \frac{\boldsymbol{m}^H p^H}{\rho^H}\right) =\\ \frac{C_0}{Pr_t \gamma M_\infty^2}\left(\nabla T^H, h^2 \rho^h |\boldsymbol{S}^h| \nabla T^h - H^2 \rho^H |\boldsymbol{S}^H| \nabla T^H\right).\end{aligned} \tag{43}$$

This equation yields

$$Pr_t = \frac{C_0}{\gamma M_\infty^2} \frac{\left(\nabla T^H, h^2 \rho^h |\boldsymbol{S}^h| \nabla T^h - H^2 \rho^H |\boldsymbol{S}^H| \nabla T^H\right)}{\left(\nabla T^H, \frac{\boldsymbol{m}^h p^h}{\rho^h} - \frac{\boldsymbol{m}^H p^H}{\rho^H}\right)}. \tag{44}$$

Mixed model

The procedure in this case is the same as for the DYSE model, except in (17) $\boldsymbol{U}' \neq 0$. In particular we get

$$C_0 = -\frac{1}{2} \frac{\left(\boldsymbol{S}^H_{dev}, \frac{(\boldsymbol{m}^h + \boldsymbol{m}') \otimes (\boldsymbol{m}^h + \boldsymbol{m}')}{\rho^h + \rho'} - \frac{(\boldsymbol{m}^H + \boldsymbol{m}'') \otimes (\boldsymbol{m}^H + \boldsymbol{m}'')}{\rho^H + \rho''}\right)}{\left(\boldsymbol{S}^H_{dev}, \rho^H H^2 |\boldsymbol{S}^H| \boldsymbol{S}^H_{dev} - \rho^h h^2 |\boldsymbol{S}^h| \boldsymbol{S}^h_{dev}\right)}, \tag{45}$$

and

$$Pr_t = \frac{C_0}{\gamma M_\infty^2} \frac{\left(\nabla T^H, h^2 \rho^h |\boldsymbol{S}^h| \nabla T^h - H^2 \rho^H |\boldsymbol{S}^H| \nabla\ T^H \right)}{\left(\nabla T^H, \frac{(\boldsymbol{m}^h + \boldsymbol{m}')(\bar{p}^h + p')}{\rho^h + \rho'} - \frac{(\boldsymbol{m}^H + \boldsymbol{m}'')(p^H + p'')}{\rho^H + \rho''} \right)}. \tag{46}$$

Where ρ', $\boldsymbol{m}'$ and p' are the fine scale variables at the h-scale and ρ'', $\boldsymbol{m}''$ and p'' are the variables at the H-scale.

References

[1] T.J.R. Hughes, L. Mazzei, and K.E. Jansen. Large Eddy Simulation and the Variational Multiscale Method. *Computing and Visualization in Science*, **3**:47–59, 2000.

[2] Y. Bazilevs, VM Calo, JA Cottrell, TJR Hughes, A. Reali, and G. Scovazzi. Variational multiscale residual-based turbulence modeling for large eddy simulation of incompressible flows. *Computer Methods in Applied Mechanics and Engineering*, 197(1-4):173–201, 2007.

[3] R. Codina. Stabilized finite element approximation of transient incompressible flows using orthogonal subscales. *Computer methods in applied mechanics and engineering*, 191(39-40):4295–4321, 2002.

[4] P. Gamnitzer, V. Gravemeier, and W.A. Wall. Time-dependent subgrid scales in residual-based large eddy simulation of turbulent channel flow. *Computer Methods in Applied Mechanics and Engineering*, 199(13-16):819–827, 2010.

[5] E.F. Lins, R.N. Elias, F.A. Rochinha, and A.L.G.A. Coutinho. Residual-based variational multiscale simulation of free surface flows. *Computational Mechanics*, 46(4):545–557, 2010.

[6] Y. Bazilevs, Hsu, M.C., Y. Zhang, W. Wang, X. Liang, T. Kvamsdal, R. Brekken, and JG Isaksen. A fully-coupled fluid-structure interaction simulation of cerebral aneurysms. *Computational Mechanics*, 46(1):3–16, 2010.

[7] V. Gravemeier and W.A. Wall. Residual-based variational multiscale methods for laminar, transitional and turbulent variable-density flow at low mach number. *International Journal for Numerical Methods in Fluids*, 65(10):1260–1278, 2011.

[8] Z. Wang and A.A Oberai. Spectral analysis of the dissipation of the residual-based variational multiscale method. *Computer Methods in Applied Mechanics and Engineering*, 199(13-16):810–818, 2010.

[9] Z. Wang and A.A Oberai. A mixed large eddy simulation model based on the residual-based variational multiscale formulation. *Physics of Fluids*, 22:075107, 2010.

[10] J. Smagorinsky. General Circulation Experiments with the Primitive Equations. I. The Basic Experiment. *Monthly Weather Review*, **91**:99–164, 1963.

[11] Yoshizawa A. Statistical Theory for Compressible Turbulent Shear Flows, with the Application to Subgrid Modeling. *Physics of Fluids*, **29**:2152–2164, 2000.

[12] P. Moin, K. Squires, W. Cabot, and S. Lee. A dynamic subgrid-scale model for compressible turbulence and scalar transport. *Physics of Fluids A: Fluid Dynamics*, 3:2746, 1991.

[13] S. Lee, S.K. Lele, and P. Moin. Eddy shocklets in decaying compressible turbulence. *Physics of Fluids A: Fluid Dynamics*, 3:657, 1991.

[14] R. Samtaney, D.I. Pullin, and B. Kosović. Direct Numerical Simulation of Decaying Compressible Turbulence and Shocklet Statistics. *Physics of Fluids*, **13(5)**:1415, 2001.

[15] R. Samtaney and D.I. Pullin. Subgrid-scale Modeling for Large-eddy Simulations of Compressible Turbulence. *Physics of Fluids*, **14(4)**:1511, 2002.

[16] T.J.R. Hughes, L. Mazzei, A.A. Oberai, and A.A. Wray. The multiscale formulation of large eddy simulation: Decay of homogeneous isotropic turbulence. *Physics of Fluids*, 13:505, 2001.

[17] B. Koobus and C. Farhat. A variational multiscale method for the large eddy simulation of compressible turbulent flows on unstructured meshes–application to vortex shedding. *Computer Methods in Applied Mechanics and Engineering*, 193(15-16):1367–1383, 2004.

[18] J. Bardina, JH Ferziger, and WC Reynolds. Improved subgrid-scale models for large-eddy simulation. In *American Institute of Aeronautics and Astronautics, Fluid and Plasma Dynamics Conference, 13th, Snowmass, Colo., July 14-16, 1980, 10 p.*, volume 1, 1980.

[19] S. Liu, C. Meneveau, and J. Katz. On the properties of similarity subgrid-scale models as deduced from measurements in a turbulent jet. *Journal of Fluid Mechanics*, 275(-1):83–119, 1994.

[20] C. Meneveau. Statistics of Turbulence Subgrid-stresses: Necessary Conditions and Experimental Results. *Physics of Fluids*, **6**:815–833, 1994.

[21] B. Vreman, B. Geurts, and H. Kuerten. Subgrid-modelling in les of compressible flow. *Applied scientific research*, 54(3):191–203, 1995.

[22] F. Sarghini, U. Piomelli, and E. Balaras. Scale-similar Models for Large-eddy Simulations. *Physics of Fluids*, **11**:1569–1607, 1999.

[23] S. Stolz and NA Adams. An approximate deconvolution procedure for large-eddy simulation. *Physics of Fluids*, 11:1699, 1999.

[24] S. Stolz, NA Adams, and L. Kleiser. An approximate deconvolution model for large-eddy simulation with application to incompressible wall-bounded flows. *Physics of fluids*, 13:997, 2001.

[25] J.A. Domaradzki, Kuo Chieh Loh, and P.P. Yee. Large Eddy Simulations Using the Subgrid-Scale Estimation Model and Truncated Navier-Stokes Dynamics. *Theoretical and Computational Fluid Dynamics*, **15**:421, 2002.

[26] T.J.R. Hughes and G. Sangalli. Variational multiscale analysis: the

ne-scale green's function, projection, optimization, localization, and stabilized methods. *SIAM Journal on Numerical Analysis*, 45(2):539, 2007.

[27] A. A. Oberai, J. Liu, D. Sondak, and T. J. R. Hughes. A residual-based eddy viscosity model for the les of turbulent flows. *in preparation.*

[28] D. Sondak and A. A. Oberai. LES models for incompressible magnetohydrodynamics derived from the variational multiscale formulation. *Physics of Plasmas*, submitted.

[29] A.A Oberai and J. Wanderer. Variational formulation of the Germano identity for the Navier–Stokes equations. *Journal of Turbulence*, 6(7):1–17, 2005.

[30] A.A. Oberai and J. Wanderer. A dynamic multiscale viscosity method for the spectral approximation of conservation laws. *Computer Methods in Applied Mechanics and Engineering*, 195(13-16):1778–1792, 2006.

[31] CG Speziale, G. Erlebacher, TA Zang, and MY Hussaini. The subgrid-scale modeling of compressible turbulence. *Physics of Fluids*, 31:940, 1988.

[32] A. Leonard and GS Winckelmans. A tensor-diffusivity subgrid model for large-eddy simulation. *ERCOFTAC SERIES*, 7:147–162, 1999.

[33] G.S. Winckelmans, A.A. Wray, O.V. Vasilyev, and H. Jeanmart. Explicit-filtering large-eddy simulation using the tensor-diffusivity model supplemented by a dynamic Smagorinsky term. *Physics of Fluids*, 13:1385, 2001.

[34] Guillermo Hauke. Simple stabilizing matrices for the computation of compressible flows in primitive variables. *Computer Methods in Applied Mechanics and Engineering*, 190(51-52):6881 – 6893, 2001.

[35] C Canuto, M.Y Hussaini, A Quarteroni, and T.A Zang. *Spectral Methods in Fluid Dynamics*, 1988.